Co-seismic landslides on the western rangefront of the Southern Alps, New Zealand, as a record of ground motion produced by Alpine Fault earthquakes

Astrid Serine Larsen Vetrhus

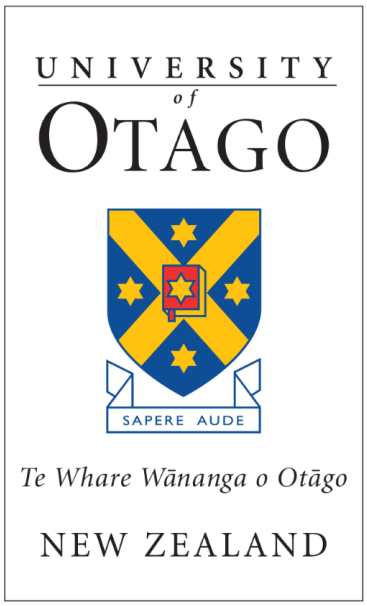

Thesis submitted for the degree of
Master of Science in Geosciences
Programme option Geohazards
60 credits

Department of Geology
Division of Sciences

UNIVERSITY OF OTAGO

and

Department of Geosciences
Faculty of mathematics and natural sciences

UNIVERSITY OF OSLO

Autumn 2017

Co-seismic landslides on the western rangefront of the Southern Alps, New Zealand, as a record of ground motion produced by Alpine Fault earthquakes

Astrid Serine Larsen Vetrhus

© 2017 Astrid Serine Larsen Vetrhus

Co-seismic landslides on the western rangefront of the Southern Alps, New Zealand, as a record of ground motion produced by Alpine Fault earthquakes

http://www.duo.uio.no/

Printed: Reprosentralen, University of Oslo

Abstract

The thesis quantifies the peak ground acceleration (PGA) required to cause large rock avalanches in the western rangefront of the Southern Alps in New Zealand, which will improve understanding of the hazard posed by co-seismic landslides in the West Coast region.

During an earthquake, ground motion can destabilize both man-made and natural structures. The Alpine Fault, which runs along the western edge of the Southern Alps and forms part of the boundary between the Australian and Pacific Plates, is a seismically active fault which appears to be in the late phase of its earthquake cycle, and a major earthquake (Mw $\geq$ 8) is expected in the near future. Seismic events are known to cause landslides in many regions of the world and are thought to be responsible for a series of large rock avalanches in New Zealand. Since large earthquake-triggered landslides often have anomalously long runouts and can induce tertiary hazards through dam breaking and subsequent flooding, they have substantial hazard potential.

The thesis quantifies the strength of PGA required to trigger large rock avalanches in the western rangefront of the Southern Alps, using published data on two particular potentially co-seismic landslides: The Round Top rock avalanche, and the Cascade rock avalanche.

Newmark's sliding block model, a permanent-displacement analysis which models a landslide as a rigid block sliding down an inclined plane, is, with some modifications introduced in this work, used to estimate the strength of PGA required to initiate these landslides. 2D static slope stability analyses are conducted using 9m and 15m resolution DEMs of the landslides, providing estimates of the Factor of Safety (the ratio between resisting and driving forces), which is then used to estimate the required strength of PGA.

The results show a median estimated lower-boundary PGA for the Cascade rock avalanche of 0.85g, with a margin of error of -0.14/+0.15 (0.71g-1g). The corresponding result for the Round Top rock avalanche is 0.92g, with a margin of error of $\pm$0.25 (0.67-1.17g). The predicted PGAs derived from these landslides will be potentially useful for constraining scenario ground motions for future Alpine Fault earthquakes.

Acknowledgements

First and foremost, I would like to thank my supervisors, Mark Stirling, Karen Mair, and Virginia Toy, for their time, (mostly) good sense of humour, and input in this project. Great thanks also to Tim Davies of Canterbury University in Christchurch, who came up with the dual-plane Newmark model, and to Nic Barth, for his suggestions on how to estimate the plane of failure parameters.

Leon Billows of the Otago University Tramping Club was a decent field assistant, cook, and GPS. General staff members at Otago's Dept of Geology, especially Luke Easterbrook, have been patient and helpful. Sarah O'Sullivan of Otago's International Office has my thanks for helping me out when I was struggling (twice). Thanks to my Kiwi friends and flatmates, both two-legged and four-legged, for all the yarns, great food, and stare-downs over who gets to sleep on my lap (done mostly by the four-legged ones). And last, but not least, thanks to my friends and family, for putting up with me running off to the other side of the planet for a year. Some of you did get a pretty sweet trip out of it, though.

Astrid Vetrhus

Contents

List of Figures

List of Tables

1 Background

1.1 Introduction

New Zealand straddles an active plate boundary; the convergence of the Pacific and Australian Plates along the full length of the country has created a diverse landscape that is geologically quite young and constantly changing.This rather precarious position is also the source of one of the greatest hazards facing modern New Zealand society. Earthquakes, and potentially earthquake-triggered geohazards such as landsliding and tsunamis, regularly cause widespread damage to life, infrastructure, and nature. Two examples of this are the 2011 M_W 6.3 Christchurch and 2016 M_W 7.8 Kaikoura earthquakes. The former caused severe damage to Christchurch's Central Business District (CBD) and surrounding areas, not least due to extensive liquefaction, leading to the deaths of 185 people. The Kaikoura earthquake occurred in a more sparsely populated area, but caused damage to houses and farmland, as well as to many structures in Wellington, about 200 km from the epicentre. The shaking also wreaked havoc on the South Island's transport system. At the time of writing, the main highway and most of the railway between Christchurch and Picton, where ferries connect to the North Island, is still closed due to the massive amount of landslide material inundating the road; it is scheduled for reopening in December 2017, a little over a year after the earthquake.

Another place where New Zealand's active tectonic environment is particularly evident is in the Southern Alps in the South Island, where the Alpine Fault, one of the major sections of the plate boundary, has uplifted the mountain range by several thousand metres. The boundary is characterized by the sharp transition from the low-lying river plains of the Australian Plate, the footwall, to the

high-relief mountains of the Pacific Plate, which forms the hanging wall. Since its formation, possibly in the early Miocene (e.g. Rupert Sutherland, Davey, and Beavan 2000), this 650 km-long, dextral strike-slip fault has accumulated a horizontal offset of about 500 km. The fault accommodates 2-3 cm of slip per year on average, but it is currently locked at shallow depths (R. Sutherland, Eberhart-Phillips, et al. 2007). The recurrence interval is 291 $\pm$ 23 years, and the last rupture occurred in 1717. That means that the fault is late in its earthquake cycle; the estimated probability of rupture, expected to reach magnitudes of M_W 7-8, is 29% within the next 50 years (Berryman, U. Cochran, et al. 2012; U.A. Cochran et al. 2017; R. Sutherland, Eberhart-Phillips, et al. 2007). An earthquake of this magnitude will have serious consequences for the areas affected, and many communities on the West Coast are likely to become devastated and/or isolated. One major hazard is the fault rupture itself, as horizontal movements of past earthquake have been shown to reach 8-9 metres (Berryman, Beanland, et al. 1992; Cooper and J. Norris 1995), another is the expected widespread landsliding due to the sharp-relief topography and tectonic weakening of the hanging wall.

However, the hazard posed by co-seismic landslides may be underappreciated; for instance, the high rates of erosion, due to the large amounts of rainfall, may quickly erase markers of landslide occurrence.A typical feature of earthquake-induced landslides is that they have long runouts (e.g. Barth 2014), which increases their area of impact. Other properties include spatial density increasing with increasing proximity to the rupture; and high, linear correlation with peak ground acceleration (PGA; Meunier, Hovius, and Haines 2007).

There is much previous and ongoing research related to the Alpine Fault to examine the properties and history of the fault, and the potential consequences of a major rupture. Examples include the AF8 project, which is a multidisciplinary research group exploring the effects a great earthquake will have on the community; the Deep Fault Drilling Project (DFDP), which involves drilling into the fault to examine its properties (e.g. Townend 2009); and paleoseismic investigations at Hokuri Creek near the south end of the fault, which has yielded a record of Alpine Fault events going back 8000 years (Berryman, U. Cochran, et al. 2012).

The strength of shaking produced by an Alpine Fault earthquake, which is of major importance when it comes to the stability both of anthropogenic and natural structures, is not well constrained, due to the lack of ruptures in modern times. Computer simulations have been carried out by the National Seismic Hazard Model (M. Stirling et al. 2012), and Bradley et al. (2017). However, there are currently no geological constraints for these simulations. The aim of this work is to estimate the minimum seismic accelerations required to cause the catastrophic failure of two pre-historic landslides, the Cascade and Round Top rock avalanches, both located in the immediate hanging wall on the western rangefront of the Southern Alps. The study utilizes a modified version of the Newmark model, a permanent-displacement analysis which models a landslide as a block sliding on an inclined plane (Newmark 1965). Slope geometry and the basal coefficient of friction control the critical acceleration, the threshold the seismic acceleration must exceed in order to promote failure. This threshold will serve as a lower-boundary estimate of Alpine Fault ground motion for the studied areas.

1.2 Landslide case studies

Co-seismic landslide hazard has historically been underestimated on the West Coast – erosion rates are high due to the large amount of rainfall, which quickly removes traces of landslide activity, and some of the deposits that have not disappeared (yet), including the two landslides used in this study, have been misinterpreted as glacial deposits (e.g. Bell and Fraser 1906; R. Sutherland, Nathan, and Turnbull 1995; Turner 1930; Warren 1967). The high erosion rates, as well as the inaccessibility of many areas due to topography and thick vegetation, means that it can be challenging to find features that may serve as records of past earthquakes.

The two landslides used in this work, discussed in detail in Sections 1.2.1 and 1.2.2, were chosen because they are reasonably well preserved, dated to within Alpine Fault events, exhibit properties indicative of an earthquake trigger, and are located in near-field (<10 km from fault trace/rupture) areas at opposite ends

of the fault. Figure 1.1 shows the location of the landslides in the context of New Zealand tectonics.

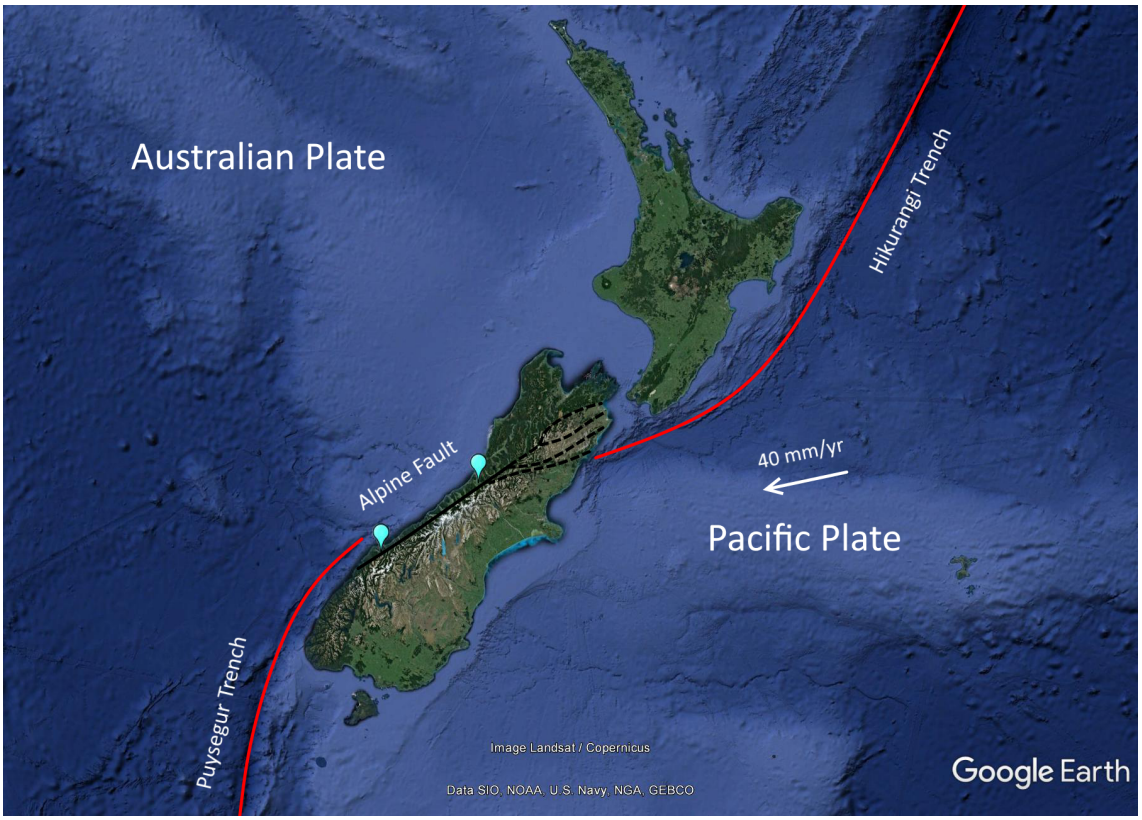

Figure 1.1: Map of New Zealand, showing plate boundary-related faults, onshore in black and offshore in red. South of New Zealand, the Australian Plate subducts under the Pacific Plate. To the north, the Pacific Plate dives underneath the Australian Plate. Locations of landslides are shown as blue markers, Cascade to the south and Round Top to the north.

These landslides are also well-studied, thanks to the efforts of Nic Barth (2014) and Craig Wright (1998), whose papers on the two landslides form the basis for the next two sections.

1.2.1 The Cascade rock avalanche

The following paragraphs are based on work done by Barth (2014), unless otherwise noted. The approx. 0.75 km^3 Cascade rock avalanche, shown in Figure 1.2, is located in the Cascade Valley, near the south end of the Alpine Fault. The source scarp is situated on the westward side of Martyr Spur, in the hanging wall directly above the trace of the Alpine Fault. The deposit covers approx. 9.1 km^2 of the gently sloping (<1°) valley floor towards the northwest, with a runout length

of 5 km and drop height of 620 m (distance from top of scarp to distal edge of deposit, and from top of scarp to lowest part of deposit, respectively). The fall line – a line connecting the centres of gravity of the scarp and the deposit – is, at 315°, nearly perpendicular to the local strike of the fault trace at 055°.

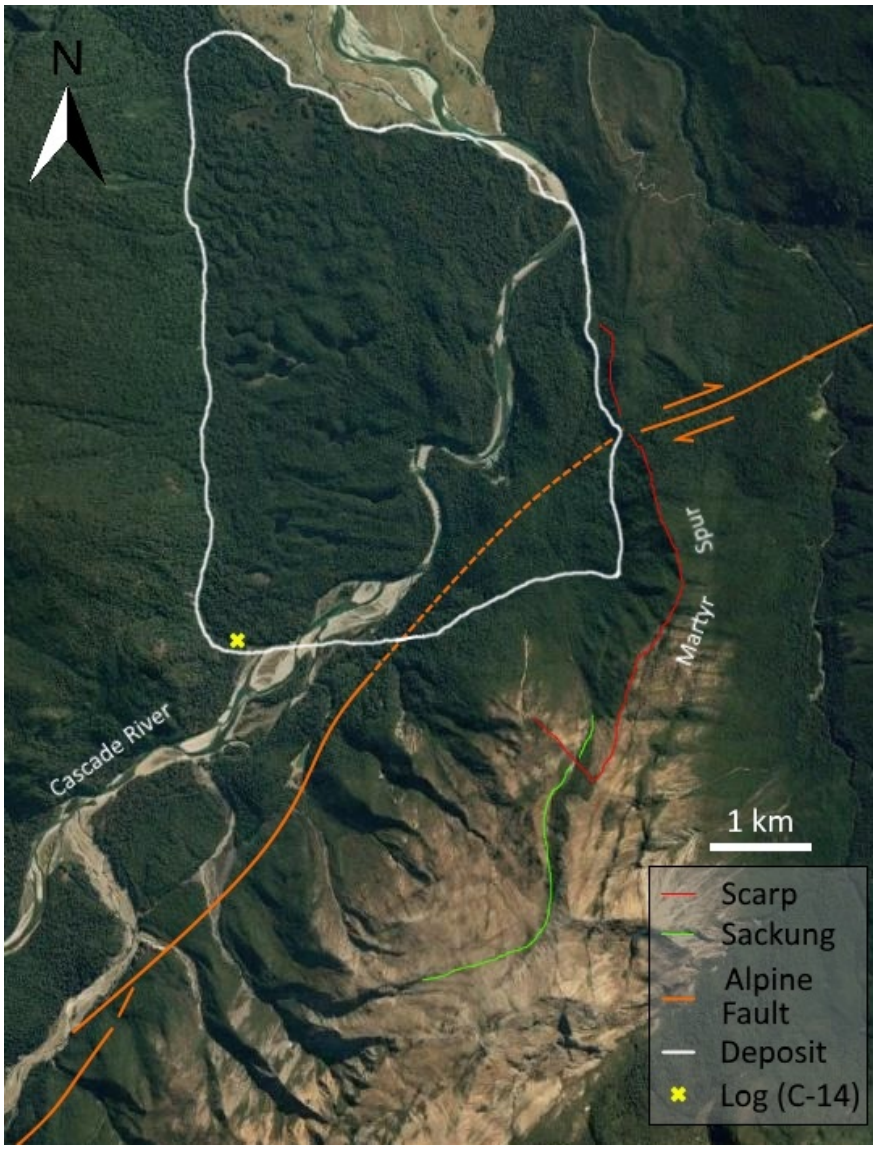

Figure 1.2: Satellite image of the Cascade rock avalanche, with annotations, after Barth (2014). The green line outlines the intersection between the sackung and remaining section; above this line, scree outlines the dip direction of the sackung. Ridge rents are seen as dark, strike-parallel lines along the top of the ridge. The yellow cross shows where the log used for dating the landslide was found. Google Earth image.

The deposit contains three different lithologies, the most prominent being the partly serpentinized peridotites of the Dun Mountain Ophiolite Belt, with occurrences of Brook Street Volcanic Group-derived mylonites from the immediate

hanging wall damage zone, and Greenland Group metasediments from the footwall. The deposit is fairly well preserved, apart from fluvial erosion by the Cascade River at the north end, which may have decreased the observable volume and runout to some degree, as well as at the base of the slope, where the river has cut a steep gorge through the deposit. The morphology of the deposit, characterized by longitudinal ridges radiating at a spreading angle of 75° and decreasing in height out from the base of the scarp, strongly suggests a single event, i.e. the entire mass was deposited in a single landslide. The best date estimate for the landslide is c. 660 (+104/–118) CE, based on the C-14 dating by Lee et al. (1983) of a log entrained in the deposit. This estimate overlaps with the 642–727 CE Hk2 earthquake event recorded at Hokuri Creek. (Berryman, U. Cochran, et al. 2012).

The landslide appears to have, at least partially, failed along existing structural weaknesses; the lower part of the slope lies within the damage zone of the Alpine Fault, and the deep-seated scarp coincides with the most prominent of several normal-sense scarps, in New Zealand termed ridge rents, lining the top of Martyr Spur. This suggests that this deep-seated gravitational slope collapse occurred along a sackung, an uphill-facing scarp often inferred to be generated and reactivated by earthquakes. Sackungen (plural; single: sackung) are a common feature throughout high-relief areas worldwide, including the Cascade Valley and the rest of the Southern Alps, where they often occur as 60°-70° dipping, ridge-parallel, uphill-facing scarps that can reach a length of more than a kilometre (Barth 2014). The Cascade sackung is shown in Figure 1.3.

They form in various ways, but are often inferred to be the result of seismic activity (e.g. Pasuto and Soldati 1996). They are also possible precursors of slope failure (e.g. Korup 2005), seen on the surface as strike-parallel scarps occurring near the top of mountain ridges.

The Cascade rock avalanche appears to have originally been part of a larger slope section with a total volume of c. 3 km^3; the remaining c. 2 km^3 section, which is adjacent to the scarp and could potentially fail in the future, has slipped more than 100 m vertically along a sackung that in total is about 5 km long, from the northern end of the landslide scarp to the south end of the remaining section. Figure 1.4 displays a modelled profile of Martyr Spur, based

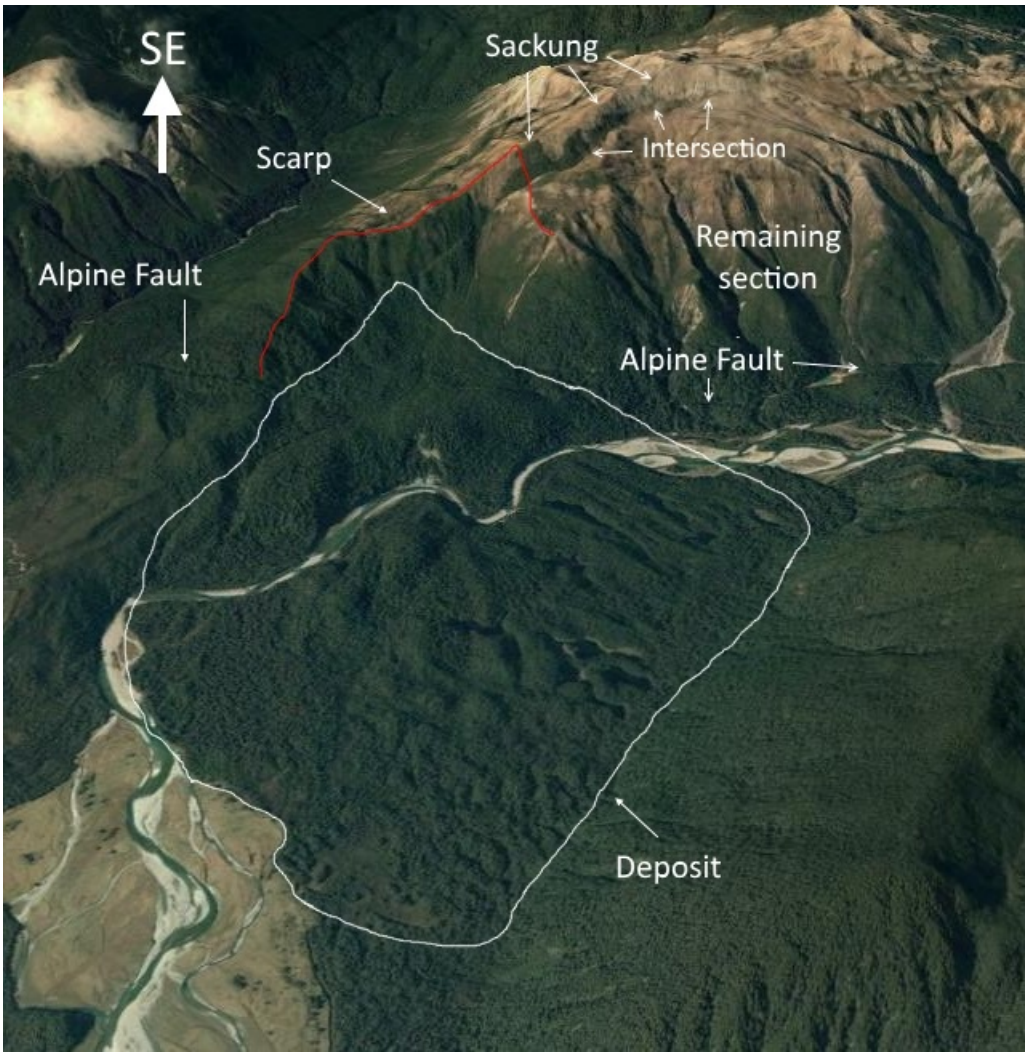

Figure 1.3: Oblique view of the Cascade rock avalanche, after (2014). The *Sackung* and *Intersection* arrows outline the visible part of the sackung above the remaining section. Google Earth image.

on field observations and aerial photos by Barth (2014), showing the internal structure of the ridge. Barth (2014) suggests that the asymmetrical distribution of the sackungen is due to topographic effects, as opposed to, for instance rock anisotropy, as gravitational collapse is more likely to face the lower elevation valley.

Sackungen have been associated with many other landslides, both elsewhere in the Southern Alps (e.g. Korup 2005) and worldwide, for instance in connection with slope failure caused by the 2008 M_W7.9 Wenchuan earthquake (Chigira, Wu, et al. 2010) and the 1999 M_W7.6 Chi-Chi earthquake (Chigira, Wang, et al. 2003).

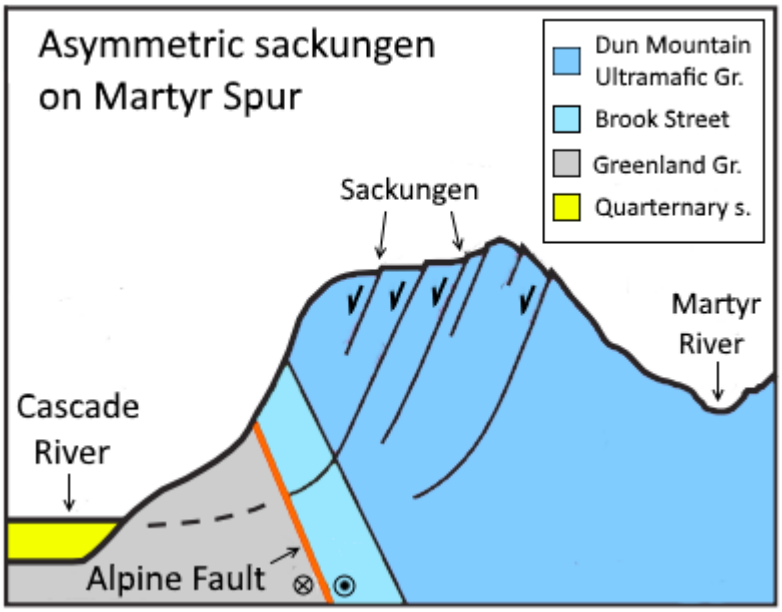

Figure 1.4: Modelled profile of Martyr Spur, after Barth (2014), showing how sackungen may propagate through the ridge. Note elevation difference of the valleys on either side.

Fieldwork

One of the main parameters of the Newmark model is the coefficient of friction. The peridotites in the Cascade area have been partly serpentinized, which poses the question of which rock type to base the coefficient of friction on – dunite or serpentinite. In the deposit, Barth (2014) observed abundant serpentinization, with antigorite serpentine coating shears and other curviplanar features. In order to estimate the degree of serpentinization of the source area, this author undertook fieldwork on Martyr Spur. The fieldwork took place near the end of January 2017, and had a duration of one day, excluding travel time to and from Dunedin, Otago.

Even at the highest visited points of the ridge, at an elevation of c. 800 m, rock outcrops were not observed; the rock is covered in scree in steep areas, and scrub in gentler dipping areas. However, serpentinite was found to be abundant in scree and creek beds, and as partly serpentinized, weathered dunite boulders. As serpentinite starts controlling frictional and rheological properties at as little as 10%-15% content (Escartín, Hirth, and Evans 2001), this work assumes that a serpentinite (antigorite) coefficient of friction is appropriate.

1.2.2 The Round Top rock avalanche

This section is built on the study of Wright (1998), as well as Barth's (2014) comparison of this landslide with the Cascade rock avalanche. The approx. 0.045 km^3 Round Top rock avalanche is situated 20 km south-southeast of Hokitika, near the north end of the Alpine Fault. The deposit covers an area of about 5.6 km^2, large parts of which have been reworked to be used as farmland. The source is a 550 m high asymmetric scarp in the hillside of Round Top, a ridge on the rangefront of the Southern Alps. Part the deposit has been alluvially reworked post-failure, forming a fan covering the base of the scarp. The surface of the talus fan is not crossed by any fault traces, suggesting that its reactivation occurred after the last rupture. The landslide consists of schist-derived mylonite and protomylonite. There is a smaller deposit immediately to the south-west; Wright termed this the southern deposit, but it is unknown if it failed at the same time as the main landslide. Figure 1.5 shows a Digital Elevation Model (DEM; acquired from Westland District Council 2017) of the landslide and surrounding areas, while Figure 1.2 shows a satellite image of the landslide.

The Round Top rock avalanche has many characteristics that are comparable with those of its southern counterpart. The trace of the Alpine Fault runs directly below the scarp; the runout and height-to-length ratio are similar, at 4800 m and 0.119 respectively; the deposit morphology is characterized by longitudinal ridges radiating out from the base of the scarp, with an estimated fall line of 334° (close to perpendicular to Alpine Fault trace at approx. 40°) and spreading angle of 90°. This landslide has also spread out over a gently sloping (1-2°) river plain without any major obstacles. Round Top is situated above a compressional segment of the Alpine Fault, which is likely causing intense shearing within the rock mass.

Yetton (1998) used C-14 dating on a log entrained in the deposit to produce an estimate of 930 ± 50 CE for the failure of the Round Top rock avalanche. Recalibration by Barth (2014) provided an estimate of 860 (+119/–95) CE, which overlaps with Yetton's estimate. Both estimates overlap with the Hk1 earthquake event (714-934 CE) recorded at Hokuri Creek (Berryman, U. Cochran, et al. 2012).

Given Round Top's asymmetry (the westward valley floor, where the

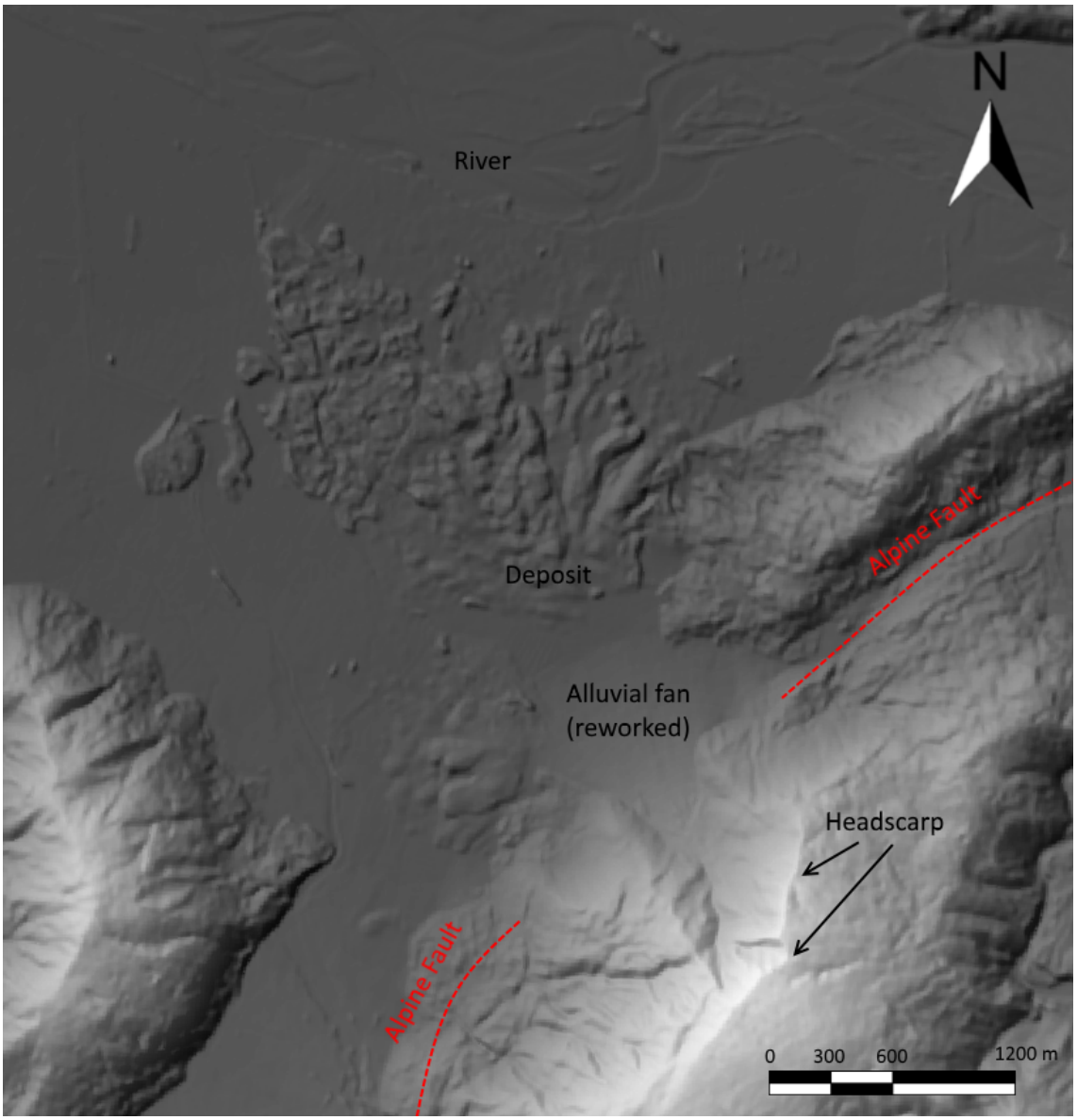

Figure 1.5: Digital Elevation Model of the Round Top rock avalanche.

landslide is located, has a lower elevation than the eastward one), close proximity to the Alpine Fault, and the strike-parallel scarps running along the top of the ridge adjacent to the major landslide scarp, Barth (2014) suggests that the failure mechanism attributed to the Cascade rock avalanche is also applicable here (Figure 1.4).

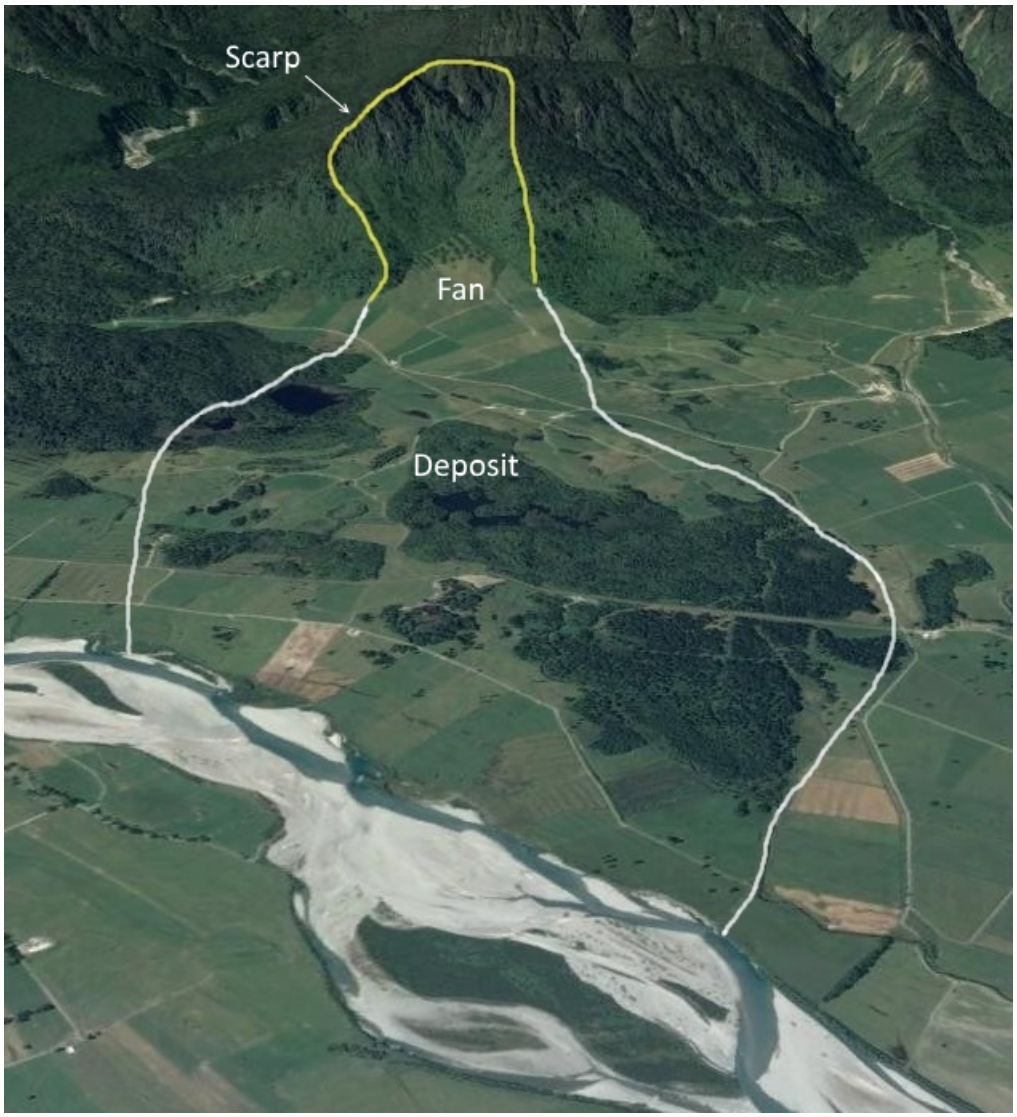

Figure 1.6: Satellite image of the Round Top Avalanche, oblique viewing angle. Google Earth image.

2 Method

This chapter is divided into three sections. The first section introduces the geomechanical landslide model underpinning the thesis, namely the Newmark model, as well as a modified version created for this study to constrain the threshold, near-field ground motions for great Alpine Fault earthquakes. The second section details spatial analysis of the Cascade and Round Top rock avalanches in ArcGIS, MATLAB and Leapfrog, a 3D-modelling software package produced by ARANZ Geo. The third section deals with application of results from the spatial analysis to estimation of the Factor of Safety (FoS, the ratio of resisting to driving forces) and the critical acceleration.

2.1 The Newmark and Modified Newmark models

2.1.1 The Newmark model

The Newmark model is a permanent-displacement analysis which models a landslide as a rigid block sliding down an inclined plane (Figure 2.1). It was conceptualized by Nathan Newmark during his 1965 Rankine lecture (Newmark 1965). In order for the block to start moving as a result of earthquake ground motion, the strength of shaking, expressed as peak ground acceleration (Jibson 2011), must exceed a critical value which depends on the Factor of Safety.

The simplest way to calculate the FoS, taking only gravity and resulting forces into account, is

$$FoS = \frac{\mu \vec{W}\ cos(\alpha)}{\vec{W}\ sin(\alpha)} \tag{2.1}$$

where FoS is the Factor of Safety, $\vec{W}$ is the weight of the landslide in N, μ is the

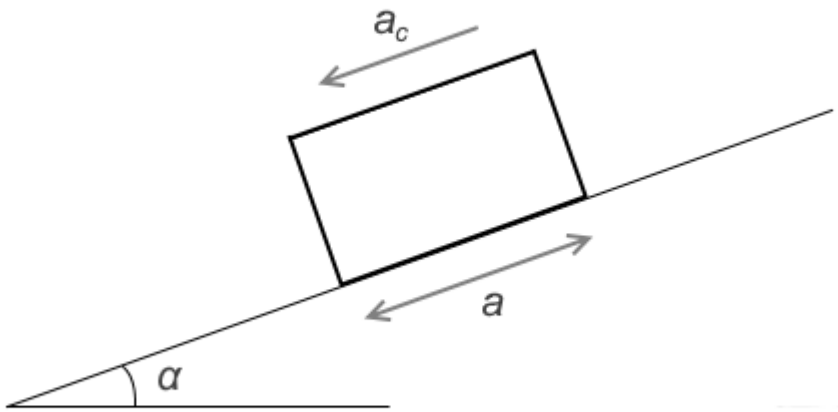

Figure 2.1: Conceptual sketch of the Newmark model, where a_c is the critical acceleration, a is the seismic acceleration, and α is the slope angle. The double-headed arrow indicates that the shaking is cyclic.

coefficient of friction, and α is the angle of the inclined plane. A simple equation used to calculate the critical acceleration is

$$a_c = (FoS - 1)g\ sin(\alpha) \tag{2.2}$$

where a_c is the critical acceleration in m/s^2 and g is the gravitational acceleration in m/s^2. A strong-motion record of the user's choice is analysed using the critical acceleration obtained from Equation 2.2. First, the part of the record which falls above the acceleration threshold is integrated, resulting in a record of velocity-time history. The duration of the latter will be different from that of the former, because inertial forces keep the block moving after the acceleration has decreased below the threshold. The velocity-time history is integrated to obtain the displacement-time history. The significance of the cumulative displacement, termed the Newmark displacement, must then be determined by the user.

The Newmark model makes several assumptions to preserve its simplicity,

the most important one being that the rheology of the block is presumed to be rigid-plastic – the block does not move if the seismic acceleration is below the critical threshold. When the threshold is exceeded, the block acts as a perfectly plastic material, deforming at a constant stress level along a defined basal surface with no internal deformation. The model also does not take vertical motion into account; only the horizontal components are included in the analysis. Four other assumptions are commonly imposed:

1. The critical acceleration is independent of strain (i.e. it is constant throughout the entire analysis).

2. Upslope resistance to sliding is infinitely large; hence, movement in this direction is prohibited.

3. The static and dynamic shear resistance are the same. Consequently, strain hardening/softening (requiring increase or decrease of stress, respectively, to keep accumulating strain during plastic deformation) is neglected.

4. The influence of dynamic pore fluid pressure is ignored.

The last assumption is a particularly important limitation on the Newmark method, as dynamic pore fluid pressure can have a significant influence on the cohesion and basal resistance of a potential landslide due to its ability to lower effective stresses (total stress minus pore fluid pressure). The local permeability will have strong influence on the pore fluid pressure, as low permeability will limit the ability of fluids to percolate through the rock, while high permeability will do the opposite. The model also does not take into account vertical ground motion and frequency distribution. The limitations will be addressed in detail in the Discussion chapter.

Both laboratory model tests (Goodman and H. Seed 1966; Wartman, Bray, and R. Seed 2003; Wartman, R. Seed, and Bray 2005) and analyses of earthquake-induced landslides (e.g. Wilson and Keefer 1983) show that the Newmark model can yield accurate predictions of slope displacement, as long as soil/rock properties, slope geometry and earthquake ground motions are well constrained.

The threshold for the critical displacement must, as stated at the beginning of this section, be set by the user. The California Geological Survey (2008)

has produced guidelines, valid for deep landslides (shallow landslides require lower thresholds), which estimate that displacements of 0-15 cm carry low probability of significant landslide events, 15-100 cm could potentially lead to strength loss and resulting failure, and 100 cm and above corresponds to a high probability of significant landslide movement. Serpentinite exhibits ductile behaviour at low temperatures (Hirth and Guillot 2013), and may therefore be able to accommodate more displacement than rocks which deform in a brittle manner at the same temperature (Jibson 2011).

This part of the model will not be considered in this work due to time limitations and difficulty finding earthquake records that would accurately represent an Alpine Fault earthquake (similar magnitude, focal mechanism, PGA levels, and with strong-motion records from near field areas). However, it represents an opportunity for future work.

2.1.2 The Modified Newmark model

The simplicity of the Newmark model is both a strength and a weakness; it is easy to apply, but may not accurately reflect real-world conditions and properties. An important example of potential mismatch between reality and model is slope geometry. Defining a single, pre-existing plane of failure for these large, complex landslides produces a rather simplified version of reality; additionally, post-failure erosion will have further complicated their geometry. While both landslides appear to have failed along sackungen, these features are unlikely to have propagated all the way to the bottom of their respective slopes, since unstable slope sections remain post-failure. If the sackung had penetrated the entire slope prior to failure, it is likely that the entire slope would have failed, instead of only a part of it (Prof T Davies, personal communication, 19-20 October 2016). It is therefore likely that the seismic shaking caused the creation of a new plane of failure extending from the tip of the sackung down to the base of the slope, allowing catastrophic slope failure to occur.

Figure 2.2 shows the fall line profile of the Cascade rock avalanche with slope angles.

The slope angle of the fall line profile decreases approximately midway down

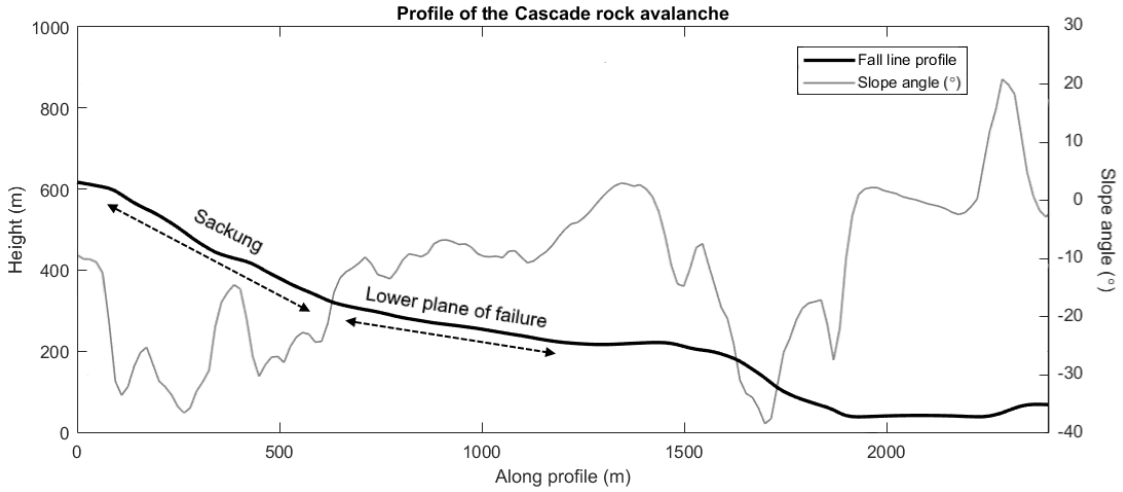

Figure 2.2: Fall line profile from the Cascade rock avalanche with slope angles. Profile height is read along the left-hand y axis, slope angles along the right-hand y axis.

the scarp, and on satellite images of the remaining section the sackung can only be traced partway down the slope (although it may be hidden by vegetation from this point downwards; see Figure 1.3). This supports the notion that the landslide dislodged itself from the sackung, and slid along a new lower-angle plane of failure.

In conclusion, simply extending the modelled plane of failure all the way to the bottom of the slope would result in underestimation of the critical acceleration, as the seismic acceleration would have had to not only initiate failure along the existing sackung, but it would most likely also have had to extend the plane of failure to the bottom of the slope. For the present scarp topography with its significant variations in slope angle, a single plane of failure is a poor approximation of the landslide geometry.

To address this issue, some modification has been introduced to the Newmark model for this study. Instead of a single plane of failure, I define two planes (Davies 2016), as illustrated in Figure 2.3.

The sackung is represented by β, while α represents the lower plane of failure connecting the sackung with the base of the slope. The dip of α is constrained by the dip of the landslide fall line profile, illustrated in Figures 2.6 and 2.7 (Nic Barth, personal communication, 21 March 2017). The addition of this lower-angle plane results in a higher critical acceleration threshold than would be acquired using the original, simple Newmark model with a single plane of failure defined

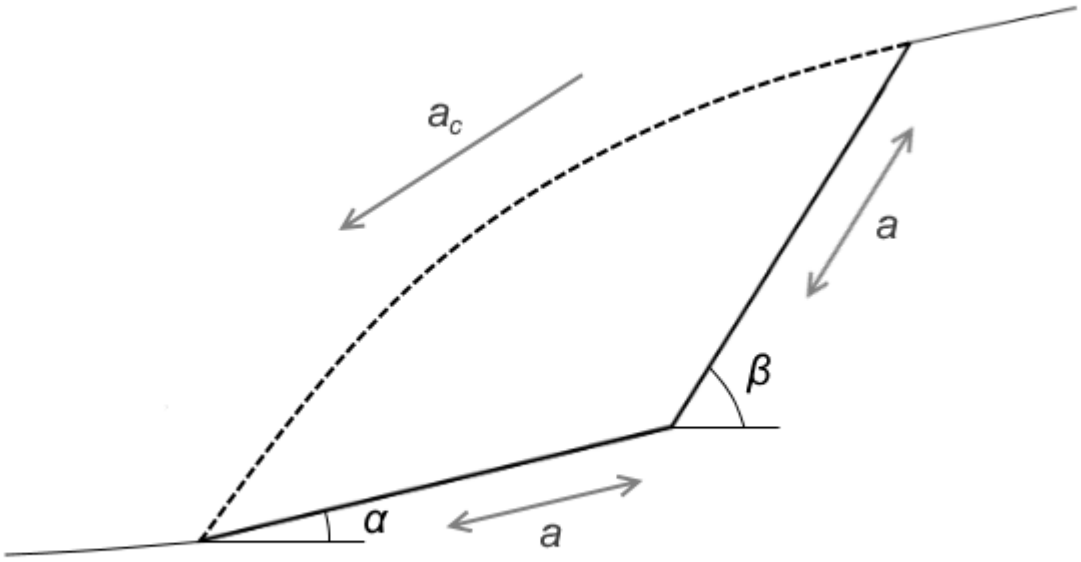

Figure 2.3: Concept illustration of the Modified Newmark model. α and β define the planes of failure. The dotted surface of the block signifies that the model does not make assumptions about the pre-failure surface geometry.

by a sackung. The new equation for the FoS is

$$FoS = \frac{\mu W\ cos(\alpha) + \mu W\ cos(\beta - \alpha)}{W\ sin(\alpha)} \tag{2.3}$$

where β is the upper slope (sackung), α is the lower slope, μ is the basal friction coefficient, and W is the weight of the landslide in N. The equation for the critical acceleration is the same as for the original Newmark model (Equation 2.2 in the previous section).

2.2 Spatial analysis

In this section, I explain how the slope geometry of the Modified Newmark model was estimated. Digital Elevation Models (DEMs) were acquired for both landslides; for the Cascade rock avalanche, the University of Otago School of Surveying's 15m national DEM was used (Columbus, Sirguey, and Tenzer 2011),

while the smaller size and more complex geometry of the Round Top avalanche warranted the use of a higher resolution DEM. A 9m DEM for the Kokatahi area was acquired from the Westland District Council (2017). The landslides were visualized in Leapfrog Geo (ARANZ Geo 2017) and ArcGIS. Profiles along of the fall lines of both landslides were extracted in ArcGIS, and exported to MATLAB, where the slope angle parameters and their margins of error were set based on plots of the profiles (Figures 2.6 and 2.7; the source code for the MATLAB scripts can be viewed in Appendices A and B). The results are shown in Table 2.1.

The Round Top avalanche has a more complex geometry compared to its Cascade counterpart (Figures 2.4, 2.5, 2.6, and 2.7), as the base of the scarp is covered by an alluvial fan, which made it difficult to determine the starting point for the basal failure surface, represented by α. Some additional profiles were extracted for this purpose, one immediately northeast of the scarp and two further to the southwest, and the surface of the substrate was extrapolated from outside the deposit, the idea being that the base of the slope is where the substrate and slope profiles intersect (Figure 2.6).

The dip of the surface of the alluvial fan changes slightly (from 16° to 9°) approximately halfway down (see fall line profile in Figure 2.6), suggesting a change in the dip of the underlying slope. This feature, as well as examination of the additional profiles, allowed a reasonable starting point of α to be chosen. The additional profiles also served as approximations of the pre-failure slope for estimation of the slope angle of α.

For the Cascade rock avalanche (Figures 2.5 and 2.7), the slope of α was set parallel to the existing lower slope of the fall line profile. The margins of error for both landslides were constrained by their geometry, which resulted in the Cascade rock avalanche having a smaller margin of error because its H/L (the centre of gravity height-to-length ratio; see Section 1.2.1) is only about 60% of that of the Round Top avalanche. In essence this means that the Cascade rock avalanche's longer runout compared to scarp height provide the angles of the margin of error with more space to spread out (for visualization, compare the x axis lengths of Figures 2.7 and 2.6).

The friction parameter, μ, was taken from existing literature, with serpentinite

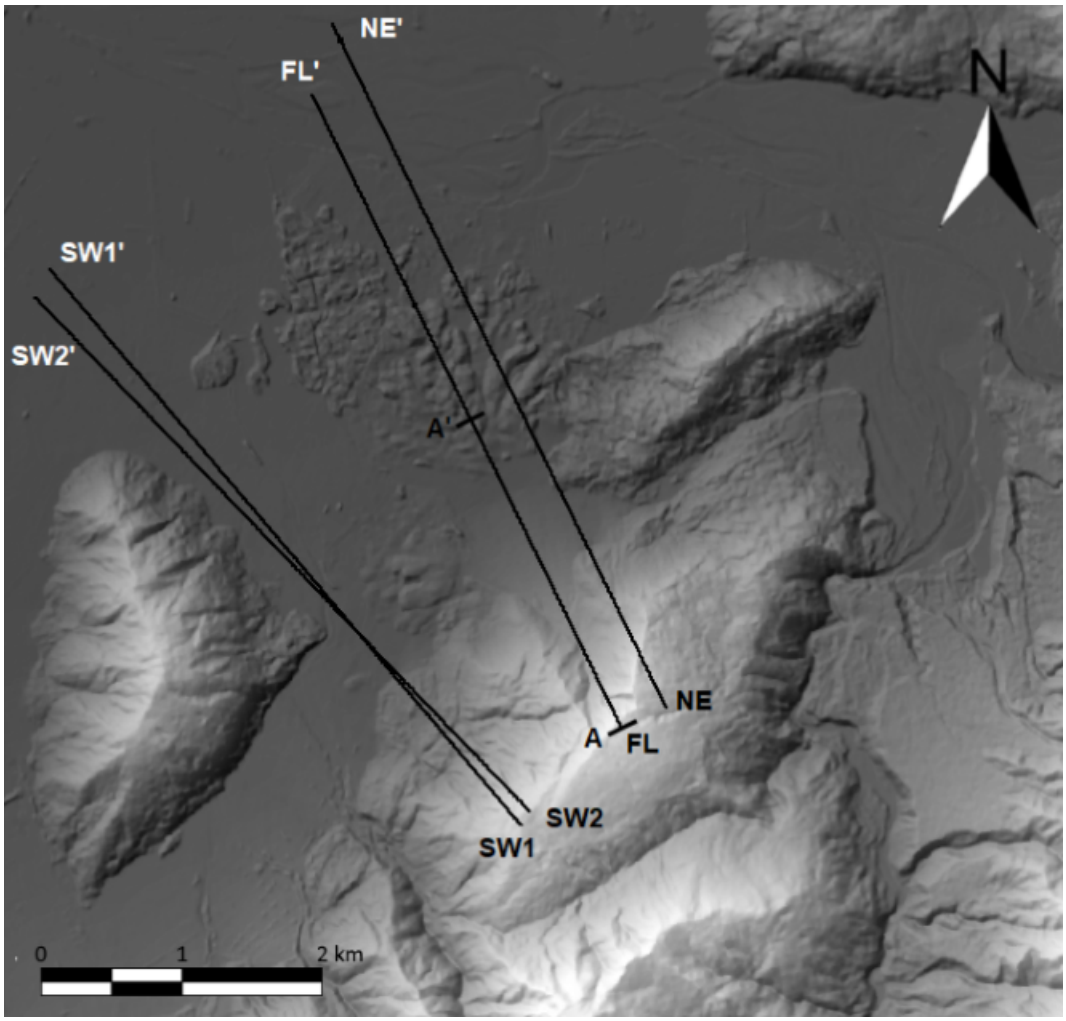

Figure 2.4: Profiles of the Round Top rock avalanche in map view, screenshot from ArcGIS. FL-FL' marks the fall line profile, NE-NE' is the northeast profile, and SW1-SW1' and SW2-SW2' are the southwest profiles. The markers A-A' on the fall line profile show the length of the profile in Figure 2.6. *I'll make the profile white if I have time.*

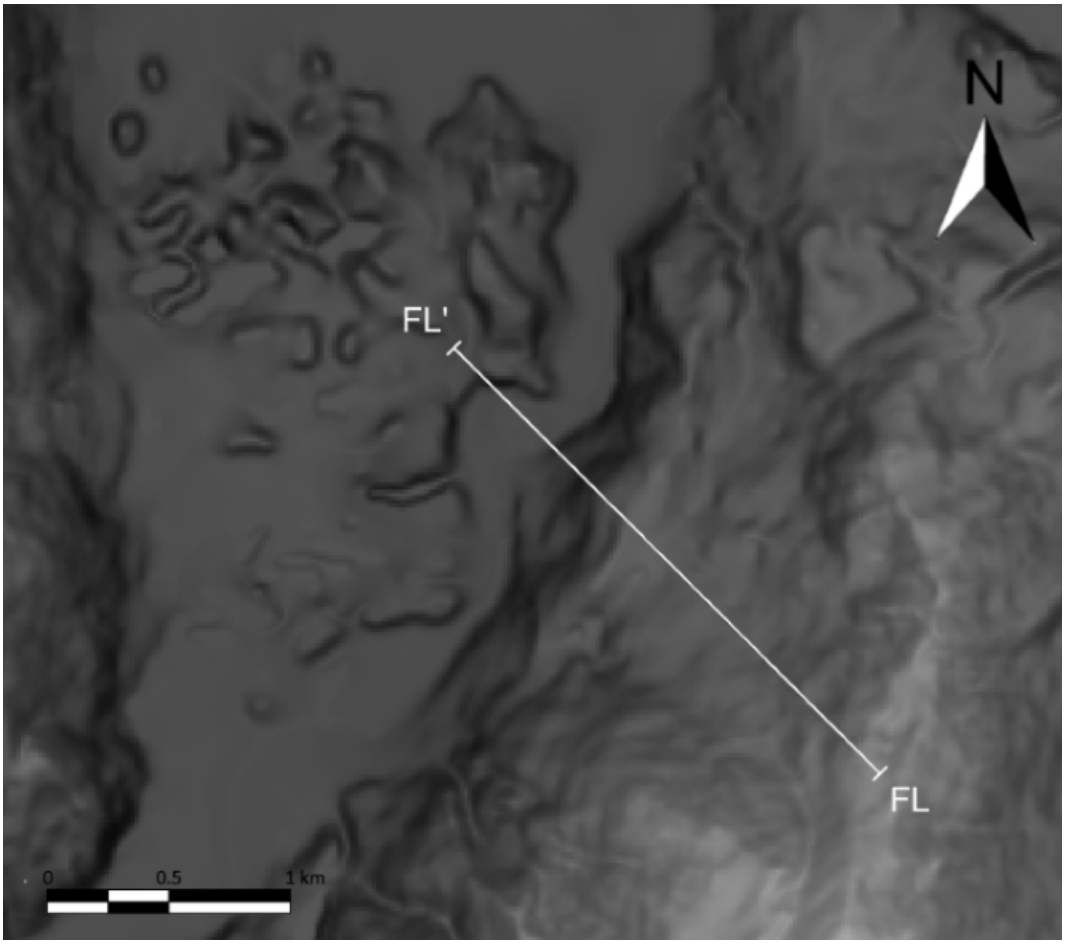

Figure 2.5: Profile of the Cascade rock avalanche in map view, screenshot from ArcGIS. FL-FL' marks the fall line profile.

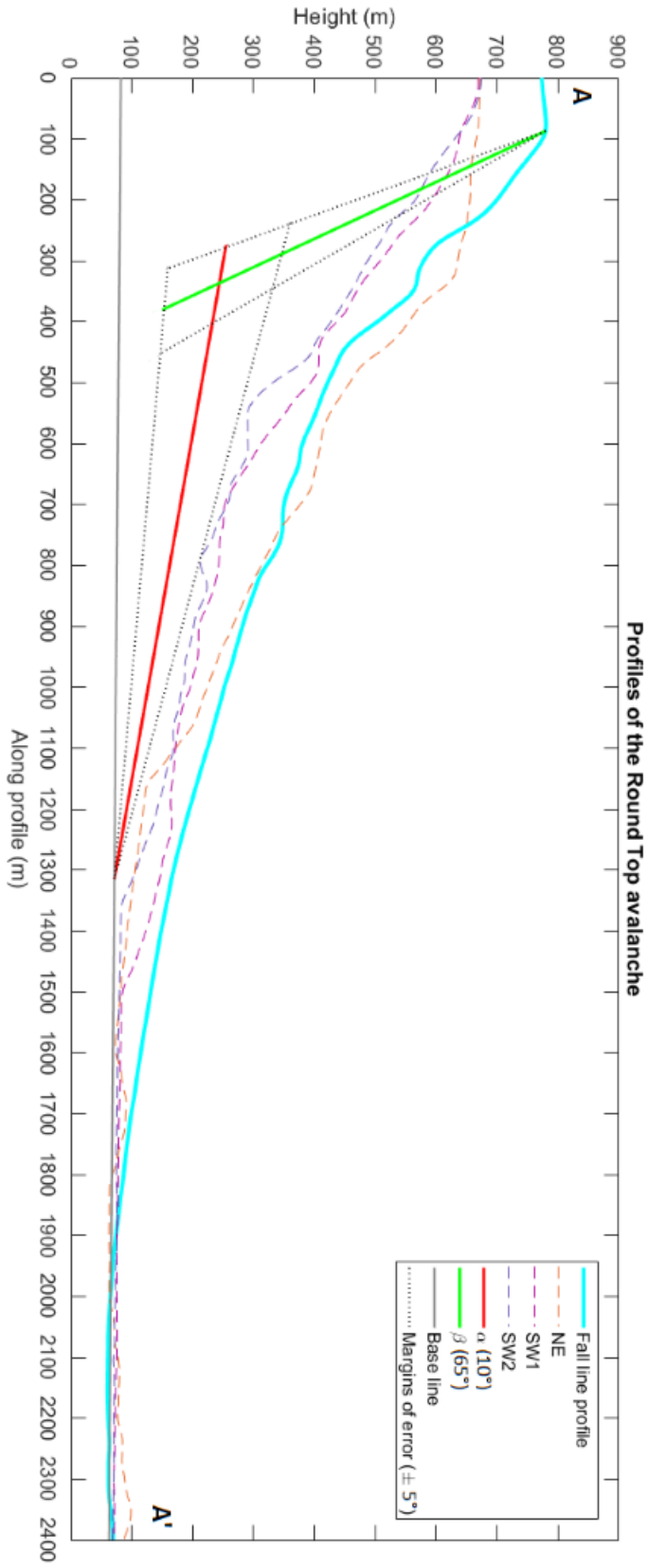

Figure 2.6: Profiles of the Round Top rock avalanche, showing the topographic profiles from Figure 2.4, and α and β with margins of error of ± 5. **A-A'** correspond to markers in Figure 2.4. α is constrained by slope geometry. Sackungen (β) generally dip 60°-70° (**??**).

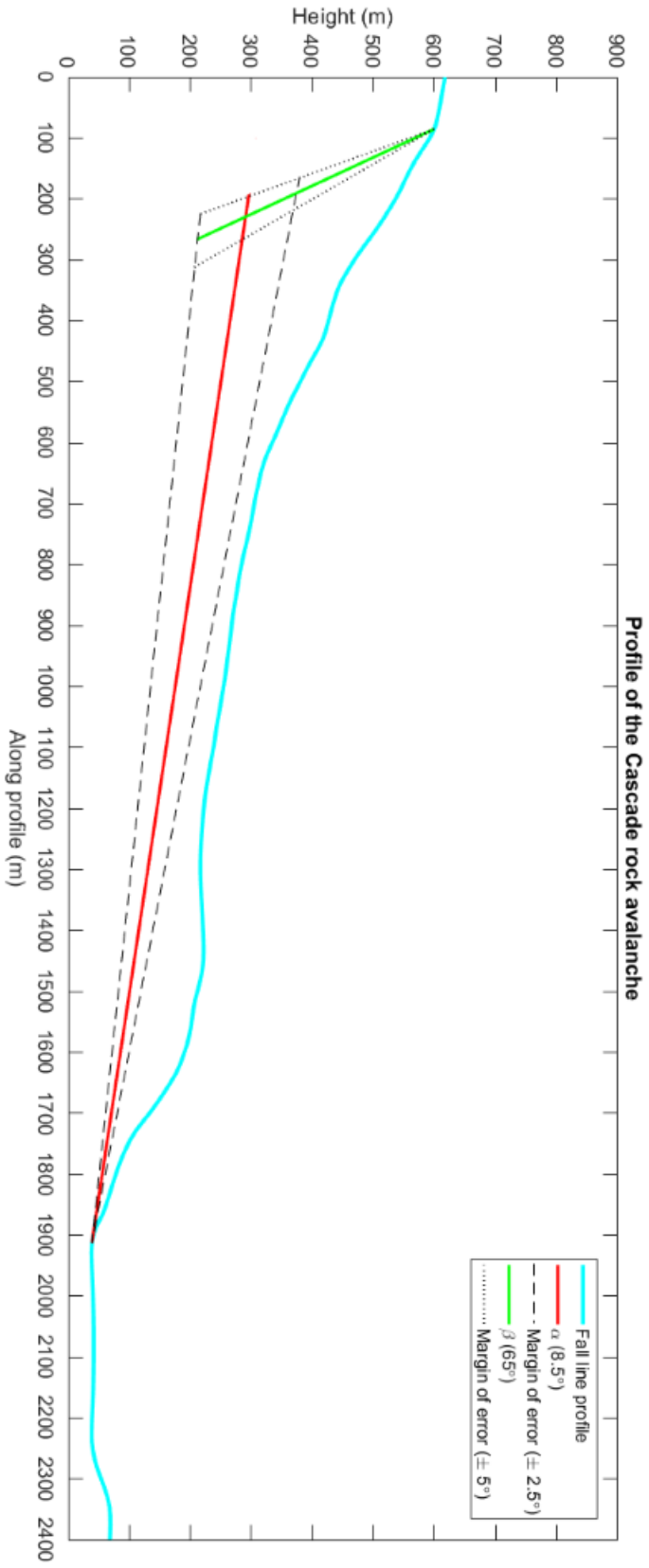

Figure 2.7: Profile of the Cascade rock avalanche, showing the fall line and α and β with margins of error ($\pm$2.5 and $\pm$5 respectively). Note that α's margin of error is half that of Round Top (Figure 2.6).

(antigorite) values from Ikari, Marone, and Saffer (2011) used for the Cascade rock avalanche due to the extensive alteration of peridotite in the area (Section 1.2.1). Typical crustal values (Byerlee 1968) were used for the schist-derived mylonite of Round Top.

Table 2.1: Variables with margins of error estimated during the spatial analysis.

	Cascade rock avalanche			Round Top rock avalanche		
Variable	α (in °)	β (in °)	μ	α (in °)	β (in °)	μ
Minimum	6	60	0.6	5	60	0.6
Median	8.5	65	0.65	10	65	0.7
Maximum	11	70	0.7	15	70	0.8

2.3 Calculating the Factor of Safety and the critical acceleration

The data obtained from the spatial analysis (Table 2.1) were used as inputs in MATLAB in order to calculate the Factor of Safety and the critical acceleration a_c, utilizing equations 2.3 and 2.2 respectively. The source code for these scripts, one for each landslide, can be found in Appendices C and D.

The independent variables, α, β, and μ, were varied one at a time according to their respective margins of error (with the others set to their respective median values) to examine each variable's influence on the results. All variables were then varied at the same time to estimate the margin of error of the Factor of Safety and the critical acceleration. The outcome of the analysis is presented and discussed in Chapters 3 and 4 respectively.

3 Results

This chapter presents the results obtained from the modified Newmark analysis – the Factor of Safety and critical acceleration estimates. Results for the Cascade rock avalanche are shown in Figure 3.2 and Table 3.2, and corresponding results for the Round Top rock avalanche are shown in Figure 3.1 and Table 3.1. Direct and inverse proportionality, where discussed, is considered within the limits (margins of error) of each variable. These terms are used for ease of understanding rather than mathematical accuracy, as most of the equations used here are not linear, but trigonometric functions with, mathematically speaking, narrow limits which in most cases allow them to approximate linearity.

3.1 The Round Top rock avalanche

Figure 3.1a shows the model sensitivity for the Factor of Safety. Exact values for the minimum, median and maximum are shown in the α, β, and μ columns of Table 3.1. α has the largest influence on the result, displaying a non-linear, inverse relationship with the FoS and producing both the largest and the smallest estimate for this figure. β exhibits inverse proportionality and has limited influence, with a total FoS range of only $\pm$ 0.25, while μ shows a slightly stronger (relative to β), directly proportional relation, producing a range of nearly $\pm$ 1.

Figure 3.1b shows the model sensitivity for the critical acceleration. Exact values for the minimum, median and maximum are shown in the α, β, and μ columns of Table 3.1. α and β display a very similar, inverse relation, with the steepest angles producing 0.87g in both cases, and the lowest 0.96g-0.97g. Compared to the other variables, μ exhibits a stronger, direct proportionality, with the highest value producing a critical acceleration estimate of >1g.

Figure 3.1c shows the estimated range of the Factor of Safety, calculated using Equation 2.3 and combining the margins of error of all independent variables. The first **Total** column in Table 3.1 contains minimum, median, and maximum values. The result is strongly non-linear due to the influence of α, and the range suggests that the slope was stable prior to the triggering event, as all values are well above the $FoS = 1$ stable/unstable regime boundary.

Figure 3.1d shows the estimated range of the critical acceleration, calculated using Equation 2.2 and combining the margins of error of the Factor of Safety and α. The second **Total** column in Table 3.1 contains exact minimum, median, and maximum values. The estimated range is approximately linear and generally fairly high, with the lowest estimate at nearly 0.7g, a median of 0.92g, and the highest estimates exceeding 1g. The range is equal to 0.92g $\pm$ 25g.

Table 3.1: Factor of Safety and critical acceleration estimates for the Round Top rock avalanche. The α, β, and μ columns show minimum, median, and maximum estimates for the model sensitivity, and the "Total" columns show the same data for the estimated ranges of the Factor of Safety and the critical acceleration.

	Factor of Safety				Critical acceleration (g)			
From figure		3.1a		3.1c		3.1b		3.1d
Variable	α	β	μ	**Total**	α	β	μ	**Total**
Minimum	12.02	6.56	5.38	**3.57**	0.96	0.97	0.76	**0.66**
Median	6.28	6.28	6.28	**6.28**	0.92	0.92	0.92	**0.92**
Maximum	4.35	5.99	7.18	**14.41**	0.87	0.87	1.07	**1.17**

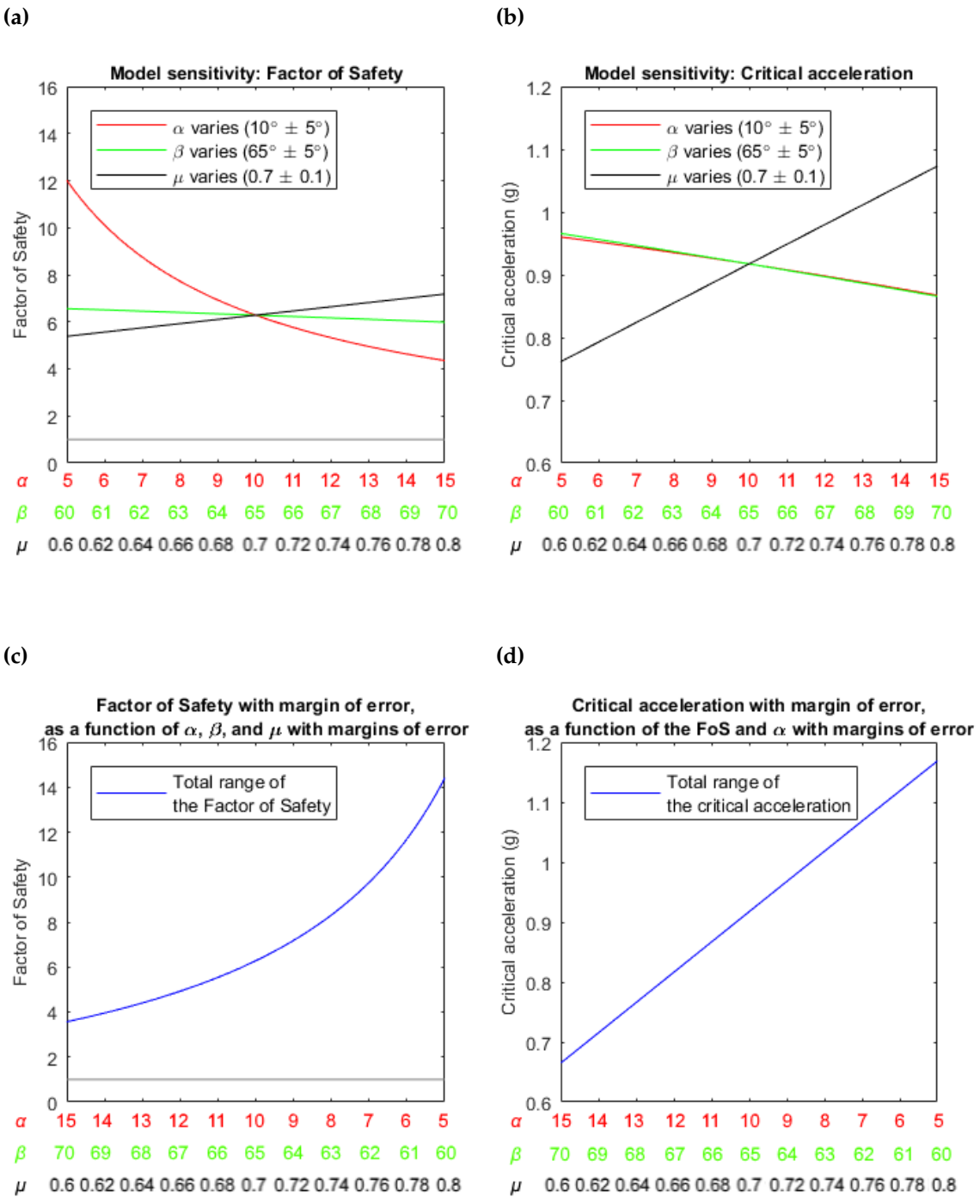

Figure 3.1: Factor of Safety and critical acceleration estimates for the Round Top rock avalanche. **(a)** Model sensitivity for the Factor of Safety. The rows on the x axis are colour coded to illustrate which graph they represent/belong to. For each function, one variable changes and the other two variables are constant and set at their median values, which are listed in the legend. The grey line represents $FoS = 1$, the boundary between the stable and unstable regimes. **(b)** Model sensitivity for the critical acceleration. The figure is read the same way as Figure a. **(c)** The Factor of Safety. The colour coded x axis illustrates how the variables relate to the FoS, e.g. that α and β have an inverse relation with the FoS. The grey line represents $FoS = 1$. **(d)** Critical acceleration. The figure is read the same way as Figure c.

3.2 The Cascade rock avalanche

Generally, the Cascade results are similar to those estimated for Round Top, except that the ranges are narrower due to the smaller margins of error for the basal coefficient of friction, μ, and the lower plane of failure, α. All Factor of Safety and critical acceleration plots share the same y axis limits, allowing for direct comparison between the landslides.

Figure 3.2a shows the model sensitivity for the Factor of Safety. Exact values for the minimum, median and maximum are shown in the α, β, and μ columns of Table 3.2. While α exhibits the strongest influence on the FoS also for this landslide, it only produces a range half that of its Round Top counterpart, due to the smaller margin of error. This is especially apparent at the top of the range, where the Cascade estimate is 9.39, whereas the Round Top equivalent is 12.02. The ranges of β and μ are similar, but a little narrower and higher than their Round Top counterparts.

Figure 3.2b shows the model sensitivity for the critical acceleration. μ exhibits direct proportionality and the strongest influence, producing a range of 0.15g. α and β share a similar, inverse influence, though α's influence is a little weaker compared to its Round Top equivalent, where α and β's influences are practically the same, which suggests that the difference between the Cascade planes is due to the lower uncertainty of α at 2.5°, as opposed to 5° for all other planes of failure.

Figure 3.2c shows the estimated range of the Factor of Safety, calculated using Equation 2.3 and combining the margins of error of all independent variables. The first **Total** column in Table 3.2 contains minimum, median, and maximum values. The estimates again suggest that the slope was stable prior to failure, with a slightly higher minimum (4.71) compared to Round Top (c. 3.57). The graph is somewhat straighter than that of Round Top due to the smaller margin of error for α, which also produces a narrower range. The median is 6.78, vs. 6.28 for Round Top. The greatest difference is found at the top of the ranges, with the Cascade maximum at 10.6 well below its Round Top counterpart at 14.41.

Figure 3.2d shows the estimated range of the critical acceleration, calculated using Equation 2.2 and combining the margins of error of the Factor of Safety

and α. The second **Total** column in Table 3.2 contains exact minimum, median, and maximum values. Following from the Factor of Safety, the range is narrower than its Round Top counterpart; the minimum is similar to that of Round Top at 0.71g and 0.66g respectively, but the difference is larger at the top of range, with a maximum estimate of 1g for Cascade and 1.17g for Round Top. The medians are also similar, with Cascade giving the lower estimate of 0.85g, and Round Top only slightly higher at 0.92g. The Cascade range is equal to 0.85g -0.14/+0.15g.

Table 3.2: Factor of Safety and critical acceleration estimates for the Cascade rock avalanche. The α, β, and μ columns show minimum, median, and maximum estimates for the model sensitivity, and the "Total" columns show the same data for the estimated ranges of the Factor of Safety and the critical acceleration.

	Factor of Safety				Critical acceleration (g)			
From figure		3.2a		3.2c		3.2b		3.2d
Variable	α	β	μ	**Total**	α	β	μ	**Total**
Minimum	9.39	7.09	6.26	**4.71**	0.88	0.90	0.78	**0.71**
Median	6.78	6.78	6.78	**6.78**	0.85	0.85	0.85	**0.85**
Maximum	5.35	6.45	7.30	**10.60**	0.83	0.81	0.93	**1.00**

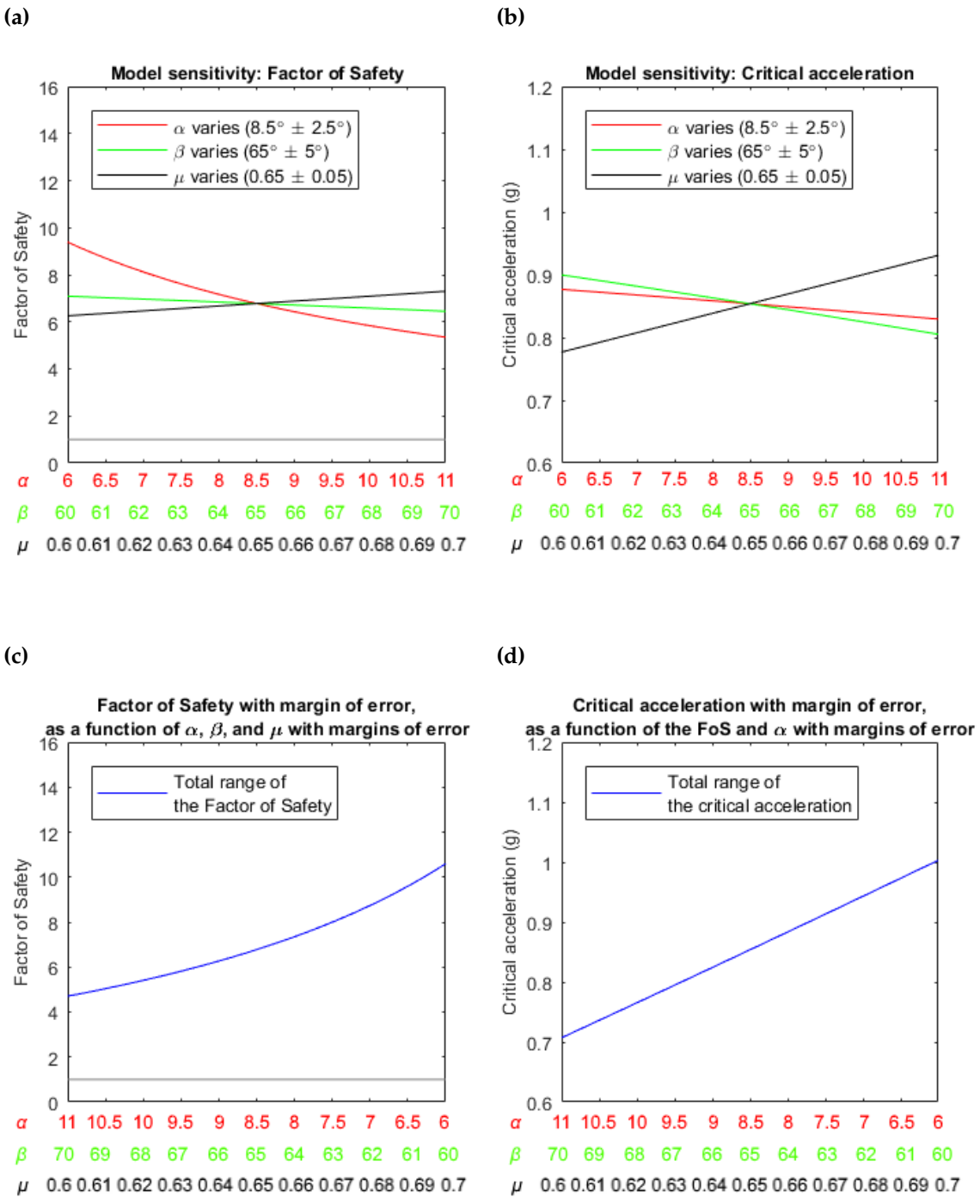

Figure 3.2: Factor of Safety and critical acceleration estimates for the Cascade rock avalanche. **(a)** Model sensitivity for the Factor of Safety. The rows on the x axis are colour coded to illustrate which graph they represent/belong to. For each function, one variable changes and the other two variables are constant and set at their median values, which are listed in the legend. The grey line represents $FoS = 1$, the boundary between the stable and unstable regimes. **(b)** Model sensitivity for the critical acceleration. The figure is read the same way as Figure a. **(c)** The Factor of Safety. The colour coded x axis illustrates how the variables relate to the FoS, e.g. that α and β have an inverse relation with the FoS. The grey line represents $FoS = 1$. **(d)** Critical acceleration. The figure is read the same way as Figure c.

4 Discussion

This chapter contains three main sections. The first section considers the performance of the modified Newmark model, including limitations inherited from the original Newmark model, which were briefly introduced in Section 2.1.1 in the Method chapter. The second section appraises the choice of landslides made for this study, taking into account dating and other properties. The third section compares the results presented in the previous chapter with existing models for prediction of Alpine Fault ground motion.

4.1 Model performance

The Newmark model is a simple analysis, which has its advantages, but also its drawbacks. Given the proper conditions (material properties, landslide geometry, etc.), the model can perform well, but can, if used under unsuitable conditions such as high-porosity rock or strain-softening soil, produce erroneous estimates. Lab results generally show high correlation with real-life events if used under the proper conditions (2.1.1). This section discusses the constraints on the model, which were briefly introduced in the Method chapter, in greater detail.

4.1.1 Pore fluid pressure

Neglecting pore fluid pressure is unwise in situations where significant dynamic pore pressure can accumulate, such as in loose sediment, permafrost or submarine slopes. In the cases presented in this thesis, which involve relatively competent, but locally highly fractured rock in a region with high levels of precipitation, the main question is whether or not the rock masses can be considered free-draining. A free-draining rock mass provides fluids with

efficient pathways along which to percolate and eventually leave the rock mass, preventing significant pore fluid pressures from building up at any one place.

The rock types present in the Cascade rock avalanche, mainly partly serpentinized peridotite, generally have low permeability (Kawano, Katayama, and Okazaki 2011; Sundberg, Hirth, and Kelemen 2010). Serpentinite permeability is non-isotropic; the rock is more permeable parallel to the fabric orientation relative to the perpendicular direction. However, at relatively shallow depths (10 MPa, approx. 400 m depth assuming lithostatic pressure), the difference is only one order of magnitude (approx. 10^{-19} m^2 vs. 10^{-20} m^2 respectively), and at surface conditions the difference has negligible effect on fluid flow within the rock mass (Kawano, Katayama, and Okazaki 2011).

Proximity to the Alpine Fault most likely increases permeability due to earthquake-induced fracturing in the fault damage zone. Barth (2014) found mylonite, belonging to the approx. 400 m thick Brook Street Volcanic Group in the hanging-wall damage zone, with predominantly foliation-perpendicular fractures both outside and within the Cascade deposit. These fractures may, depending on dip, also decrease slope stability.

Sutherland (2012) estimated bulk permeability values of $>10^{-14}$ m^2 for hanging-wall ultramylonite 50 m from the PSZ during DFDP-1B drilling at Gaunt Creek, about 80 km southwest of Round Top. Cox (2015) inferred a fracture permeability of $10^{-15} - 10^{-12}$ m^2 based on regional observations from Otago (a region on the eastern side of the Main Divide) and the Southern Alps, concluding that these values are comparable to those estimated for the ultramylonite. The bulk permeability is therefore likely to be similar in the Round Top source area mylonites, which are located <1.5 km from the fault trace.

The sackungen provide another pathway for water into the rock and there is likely to be an extensive fracture network in the area around the sackungen. During fieldwork carried out for this work, the Cascade landslide sackung (Section 1.2.1) was found to host a creek which in some places flows on the surface and in some places underground, before it eventually reappears on the surface to join other creeks, and finally the Cascade River. The creeks in the scarp itself run at the bottom of gullies, which are generally 2-3 m in depth and at most up to

approx. 5 m deep. This amount of erosion suggests that they have followed their present course for a substantial period of time. There are also several ridge rents on the other side of Martyr Spur (relative to the location of the scarp), visible in satellite photos (1.2).

To summarise, the landslides are thought to host a well-developed fracture network, consisting of sackungen and related fractures and the Alpine Fault hanging-wall damage zone. Water follows well-developed paths both on the surface and through the underground fracture network. Hence, the rock mass is assumed to be free-draining.

4.1.2 Strain softening and hardening

The Newmark model does not take strain softening or hardening into account; it considers the landslide block as a perfectly plastic material. Near-surface conditions generally do not promote strain hardening, but it may occur under certain conditions.

At low confining pressure, it is generally easier to slide over asperities than to break through them. Strain hardening, which is caused by particles interlocking under stress, increasing the strength of the rock mass and thus its resistance to shear (Byerlee 1968; Fossen 2010), is therefore limited in this stress regime. The presence of water also limits strain hardening by reducing effective stress and lubricating surfaces (Morrow, Shi, and Byerlee 1982), making deformation along existing fractures more likely to occur as brittle (though water may also promote strain softening). High strain rates like those expected during catastrophic slope failure tend to promote strain hardening (Romeo 2000), and the creation of a new plane of failure, α, is likely to involve some plastic deformation, and therefore possibly strain hardening, before rupture. These strength variations with slip are poorly defined for the rocks discussed in this thesis; hence, the potential impact of strain hardening and softening is unknown. However, even if it could be taken into account, the occurrence of strain hardening would increase the critical acceleration, as it would increase the amount of stress and therefore shaking required to produce failure. As such, the lower-boundary ground acceleration estimate that this work is concerned with is not affected by the omission of the

effect of strain hardening.

4.1.3 Evolution of the critical acceleration

The Newmark model assumes that the critical acceleration is independent of strain, and thus constant throughout the analysis. In this work, the controlled parameters affecting the critical acceleration are plane of failure orientations and the basal coefficient of friction. As considered in the following paragraphs, the coefficient of friction may change as the velocity changes during landslide initiation, which will in turn affect the critical acceleration.

Handwerger (2016) employs a rate-and-state model, typically used for fault modelling, to explain the frictional behaviour of both catastrophically failing and slow-moving landslides. The rate-and-state model, described in detail elsewhere (e.g. Scholz), explains how the coefficient of friction, μ, responds to a change in sliding velocity (V_1 to V_2, where $V_2 > V_1$ and $V_1, V_2 \neq 0$). μ initially holds some steady-state value, until the instant the velocity changes, when it increases rapidly (the rate effect), before it slowly evolves to a new steady-state value (the state effect). Rate-weakening behaviour implies that the new steady-state value is lower than the initial steady-state value; the opposite is the case for rate-strengthening behaviour. Faults that display rate-weakening behaviour accommodate displacement via earthquakes, whereas rate-strengthening properties are associated with creep. Analogously, catastrophically failing landslides exhibit rate-weakening friction, whereas slow-moving landslides exhibit rate-strengthening friction. As the Cascade and Round Top rock avalanches are landslides that have failed catastrophically, it can be surmised that their materials exhibited rate weakening behaviour at the time of failure. Generally, serpentinite exhibits rate strengthening behaviour below a shear rate of c. 0.1 m/s; above this value, the mineral rapidly loses strength (Kohli et al. 2011). At the initiation of a rock avalanche, high acceleration causes a rapid increase in velocity, meaning that this shear rate threshold will be exceeded quickly. As velocity has a direct impact on strain, it can be concluded that the critical acceleration is dependent on strain due to its relation with velocity and the coefficient of friction.

To summarize, the coefficient of friction was most likely not constant throughout initiation of failure, causing the friction-dependent critical acceleration (Equations 2.1 and 2.2) to change as a result. However, in order to initiate failure, the seismic acceleration must still have exceeded the constant critical accelerations calculated in this work, so ground motions are still likely to have exceeded this level for some amount of time. This limitation does mean that Newmark displacements may be underestimated, as the decreasing critical acceleration results in progressively larger parts of the seismic record exceeding the threshold.

4.1.4 Frequency distribution

The highest PGAs in an earthquake strong-motion record are generally on the higher end of the frequency spectrum; long-period motion is thus often underrepresented by the Newmark model, depending on the value of the critical acceleration. An Alpine Fault earthquake with an estimated magnitude of $M_w 7-8$ and probable duration of 1-2 minutes will produce a wide range of frequencies, which will have varying impacts on slope stability.

High- and low-frequency motion may impact (slope) stability in different ways not always foreseen by PGA-based hazard and risk analyses, as seen to devastating effect during the February 2011 Christchurch earthquake. During rupture, ground motion rich in frequencies close to the fundamental frequency of the thick surface soil deposits caused resonance, which led to more severe liquefaction than predicted by PGA levels alone (Tsaparli et al. 2016). In general, PGA is considered a controlling parameter for landslide initiation, but long-duration shaking may have an even greater impact on slope stability (Hancox, Perrin, and G.D. 2002). However, taking frequency content into account is beyond the scope of this work.

4.1.5 Sackung propagation and slope geometry

Unlike the previous sections in this chapter, which concern both the original and modified Newmark models, this section is solely a consideration of aspects related to the modified Newmark model; the two planes of failure defined in the modified Newmark model are a result of the progress of sackung propagation

at the time of failure. Sections 1.2.1 and 2.1.2 introduce and discuss this concept using the Cascade rock avalanche as an example, before the concept is applied to Round Top. In short, it is surmised that the sackung had only partially penetrated the slope prior to failure, which probably led to only a smaller section of the slope actually failing, as penetration all the way to the base of the slope would likely have resulted in failure of the entire volume. According to the model, the resulting landslide would have dislodged from the sackung, β, while a new, lower-angle plane of failure, α, ruptured to link the bottom of the sackung to the base of the slope, allowing the rock mass to slide along this new plane (Figure 2.3).

Sackung formation is common throughout the Southern Alps, and there is clear evidence of sackung formation in the Cascade Valley (Section 1.2.1), where vertical displacements of more than 100 m can be observed adjacent to the Cascade rock avalanche along the approx. 5 km long sackung that extends along Martyr Spur and coincides with the long axis of the scarp. Barth also made observations of sackung formation for the Round Top scarp (Section 1.2.2).

If the sackung had penetrated the full height of the slope, it would have formed a strong pre-existing structure along which failure could have occurred for the entire slope, as initiation would likely have required less severe shaking compared to the most likely state with only partial propagation, which requires the rupture of a new plane of failure. The modified Newmark model itself does not distinguish between these two scenarios beyond the shape of the failure surface; the geometry of the model would therefore also constitute a rough approximation of a rotational slide.

The upper part of the scarp, where the sackung is used as the plane of failure, dips at approx. 30°, as opposed to the 60°-70° dip used in the calculations (Section 2.1.2). The cause of this discrepancy is likely mass movement; the sackung scarp above the remaining slope section (the section that has not failed, but has slid along the sackung), adjacent to the now-vegetated Cascade scarp, is covered in scree and there are many large boulders lying where the slope flattens out at the top of the remaining section. This suggests a high degree of erosion as a result of mass movement, with the result being a decrease in slope angle. This

may have occurred during and/or after the main landsliding event. It is also probable that some deposits remain on the scarp, thereby obscuring the scarp itself and decreasing the slope angle. Barth (2014) found that sackungen scarps at Martyr Spurgenerally dip around 60°. This is an area that, with its westward orientation (towards the primary wind direction), high elevation, and lack of vegetation, is very exposed to wind and precipitation, which tends to hasten erosional processes; this is also the case for Round Top, where Barth (2014) observed ridge-parallel sackungen similar to those in the Cascade Valley.

The lower part of the scarps is less exposed to erosion due to its lower slope angle, lower elevation, and thick vegetation. At the age of the landslides (1000-1500 years), and the scale apparent in the slope profiles (100s of metres; see Figures 2.6 and 2.7), it would take a high rate of erosion to significantly alter this part of the scarp post-failure. A large amount of landslide material was likely deposited here (Barth 2014); this could potentially decrease the slope angle, and hence impact the topography-constrained upper margin of error for α. The median of α is set parallel to the existing slope, while the margin of error is constrained by the slope angle (i.e. the plane cannot be situated above the current topography; see Figure 4.1).

4.2 Choice of landslides

This section considers aspects related to the landslides themselves, including possible triggers, structural priming, and local ground motion effects.

4.2.1 Trigger

The Cascade and Round Top rock avalanche are both presumed to have been co-seismically triggered, based on prior work by Barth (2014) and Wright (1998).

The best date estimate for the Cascade rock avalanche is c. 660 (+104/-118) CE, based on the C-14 dating by Lee et al. (1983), of a log entrained in the deposit. This estimate overlaps with the 642–727 CE Hk2 earthquake event recorded at Hokuri Creek. (Berryman, U. Cochran, et al. 2012), and also with c. 630 megaturbidite event recorded in Lake Mapourika sediments 160 km NE of

the Cascade Valley (Howarth et al. 2012).

Barth (2014) makes the case for a co-seismic trigger based on e.g. these dating properties, and the proximity to the fault.However, Barth (2014) notes that a rainfall trigger cannot be excluded, which is also the case for Round Top.

Yetton (1998) used C-14 dating on a log entrained in the Round Top deposit to produce an estimate of 930 ± 50 CE for the failure of the Round Top rock avalanche. Recalibration by Barth (2014) provided an estimate of 860 (+119/-95) CE, which overlaps with Yetton's estimate. Both estimates overlap with the Hk1 earthquake event (714-934 CE) recorded at Hokuri Creek (Berryman, U. Cochran, et al. 2012).

Hokuri Creek is almost 300 km southwest of Round Top; however, Alpine Fault ruptures have seen shown to have propagated to at least such lengths in the past – the 1717 event is estimated to have ruptured 300-500 km of the Alpine Fault (e.g. R. Sutherland, Eberhart-Phillips, et al. 2007). The date estimate also coincides with a 965-887 CE Lake Paringa megaturbidite event (Howarth et al. 2012), 170 km southwest of Round Top.

An inventory of all known historical earthquake-triggered landslides in New Zealand by Hancox et al. (2002) shows that landslides with a volume greater than 0.1 km^3, such as Cascade, occurred only as a result of earthquakes of $M_w > 7.6$ and MMI IX or higher, which probably excludes all faults on or near the south part of the South Island apart from the Alpine Fault and the Puysegur subduction zone (Barth 2014; Cox, M.W. Stirling, et al. 2012). The latter has produced several M_W 7+ earthquakes over the past few decades, but the closest structure related to the subduction zone is >40 km away, which somewhat diminishes its likelihood of being the trigger for Cascade.

The Round Top rock avalanche, at 0.045 km3, is below Hancox's (2002) threshold. Situated in the region where the Marlborough Fault Zone splays out from the Alpine Fault, there are other possible seismic sources in the area. The >200 km-long Hope Fault, which is thought to be the continuation of the plate boundary and branches off the Alpine Fault c. 30 km northwest of Round Top, is one possible trigger. So is the Poulter Fault, which was the source of the 1929 M_W 7.0 Arthur's Pass earthquake, and is situated about 50 km to the east. This

earthquake triggered the 55 million m^3 Falling Mountain landslide, the largest recorded single co-seismic landslide in the South Island (Korup, McSaveney, and Davies 2004).

In summary, an Alpine Fault trigger for both landslides is considered a fair assumption, based on properties such as dating overlaps with Alpine Fault events and other mass movement events, proximity to the fault, and size of the landslide. However, other triggers, either seismic or weather-related, cannot be excluded.

4.2.2 Structural priming of the rock mass

Structural priming is an important aspect of landslide hazard assessment. Whether a slope is stable, or "ready to go", prior to a seismic event, has a large impact on the intensity of shaking required to bring it down.

There is structural priming associated with both landslides used in this study – the sackungen in the upper parts of the slope, and the Alpine Fault damage zone in the lower parts, which create structural weaknesses that appear to have played a key role in the initiation of these landslides. Both landslides contain at least some mylonite, but the foliation is in both cases (sub-)parallel to the Alpine Fault (Cascade: Barth 2014; Round Top: Nathan, Rattenbury, and Suggate 2002), i.e. perpendicular to slope topography, which means that slope stability is largely unaffected by the foliation-related strength anisotropy.

The modified Newmark model gives high to very high estimates for the Factor of Safety, with the lowest values between 3 and 4, suggesting that the landslides were quite stable before the triggering event. The hyperbole shape of the graphs in Figures 3.1c and 3.2c, which is caused by the "inversely proportional" influence of α, suggest that it would require a significant increase of the upper margin of error of this parameter to decrease the lowest Factor of Safety estimates towards 1, the boundary between the stable and unstable regimes. Such a magnitude of increase is unlikely, as the angle of α is constrained by slope topography and even slight changes in the margin of error produce large effects due to the length of the profile, as shown in Figure 4.1, where a margin of error of +5 puts the deep-seated plane of failure at a maximum of about 30 m above current slope topography.

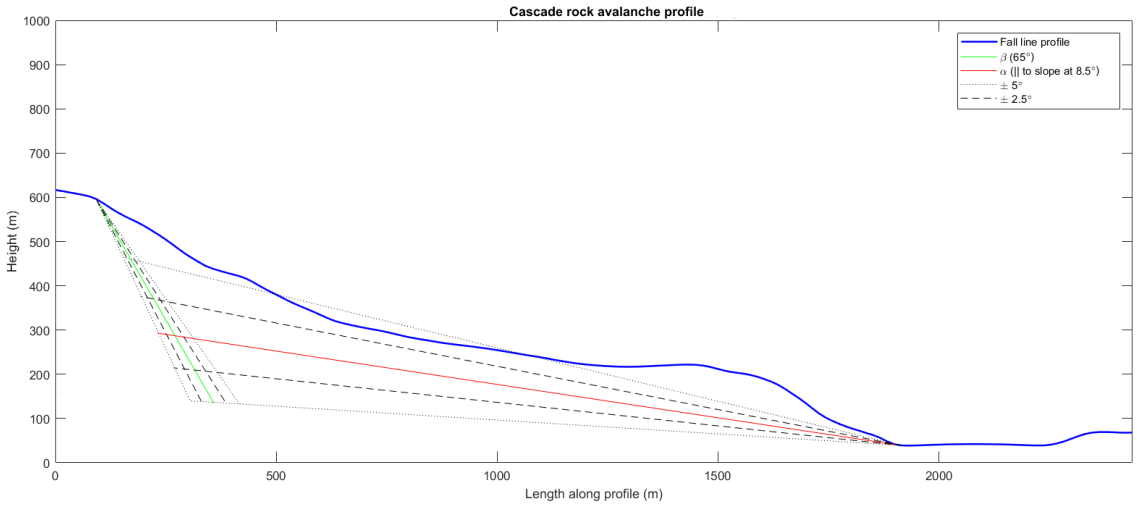

Figure 4.1: Fall line profile of the Cascade rock avalanche, with α displayed with an outer margin of error of ± 5 in addition to $\pm$ 2.5, the margin of error used in the modified Newmark model.

Given the age of the landslide (c. 1400 years) and the low slope angle associated with α, this amount of post-failure erosion is unlikely. Hence, the upper constraint on α supports the lowest estimates for the Factor of Safety, suggesting that the slope was stable prior to the triggering event.

4.2.3 Local ground motion effects

Ground motion intensities can vary significantly from site to site during a single earthquake. Factors which influence ground motion, in this study represented by PGA, generally include source parameters such as sense of slip and fault length, path effects such as rock type and travel distance, and site effects such as local topography and sediment cover. Here, some of these factors are considered in relation to the areas studied in this work.

The areas in question are both near-field and in the hanging wall, which means that they are likely to experience some of the highest PGAs caused by an Alpine Fault earthquake. The travel path will be short, which lessens the amount of geometric spreading before arrival. The source areas being in the hanging wall means that they will be subjected to stronger ground motion, relative to the footwall at the same distance from the fault trace, due to the hanging wall effect, a phenomenon caused by the smaller rupture distance (the smallest distance between the fault rupture plane and a point on the surface) observed on the

hanging wall side of a dipping fault (e.g. Donahue and Abrahamson 2014).

The travel direction of the rupture can have a substantial impact on shaking intensity at a particular site; locations near the rupture's path often experience stronger shaking compared to locations at the same distance from the fault trace, but outside the direction of travel.Bradley et al.'s (2017) PGV-based (peak ground velocity) ground motion simulations for an Alpine Fault earthquake defines three different scenarios based on hypocentre location; the northern and southern hypocentre scenarios show some difference in estimated shaking intensity for the Round Top area, with an estimated MMI 8-9 for the northern hypocentre scenario compared to MMI 9-10 for the southern one, using the PGV-MMI relation of Worden et al. (2012). The central hypocentre scenario also yields MMI 9-10. For Cascade, the estimates are all equal at MMI 8-9.

4.3 Evaluation of results

This study provides the first ground motion estimate for an Alpine Fault earthquake based on geological constraints, rather than computer simulations. Such simulations include the National Seismic Hazard Model for New Zealand (NSHM; 2010 update in M. Stirling et al. 2012), which is a probabilistic seismic hazard model; and Bradley (2017), which is a recently published PGV-based ground motion simulation. The next paragraphs compare the results of the latter, as well as findings from Hancox, Perrin, and G.D. 2002's study of coseismic landsliding occurrence in New Zealand, with the PGA estimates calculated in this work. The main areas considered are the areas around the two landslides, at opposite ends of the Alpine Fault; existing model estimates for the central part of the fault are included for comparison, but as PGA varies from location to location, the results from this work cannot be directly applied to this region.

Bradley et al. (2017) defines three rupture scenarios, distinguished by hypocentre location; one near the south end of the fault, one near the north end, and one in the centre. The study is PGV-based, but uses the one-to-one relationship with the Modified Mercalli Index Scale defined by (2012) to create estimated MMI maps for the South Island. The estimates vary spatially

depending on hypocentre location, so the study also combined the three scenarios into one figure, producing a map of maximum MMI estimates. This map shows MMI 8-9 (approx. 0.4g-0.75g according to the PGA-MMI correlation defined by Worden et al. 2012) for the Cascade area, MMI 9-10 (approx. 0.75g-1.32g; Worden et al. 2012) for the Round Top area, and MMI 8-9 for most of the central part of the fault, with MMI 7-8 (approx. 0.2g-0.4g; Worden et al. 2012) in some locations.

For the Round Top area, these estimates are in good agreement with estimates from this thesis; using the full range of the critical acceleration outlined in the Results chapter (0.66g-1.17g; Figure 3.1d) and the PGA-MMI correlation established by (2012), yields MMI 9-10. The agreement is somewhat poorer for the Cascade area, however, with an estimated critical acceleration of 0.71g-1g also corresponding to MMI 9-10 (1g yields approx. MMI 9.5), compared to Bradley's MMI 8-9.

The MMI scale for New Zealand used and adapted in Hancox (2002), based on historical earthquakes and coseismic landslides in New Zealand, suggests to this author that the case study areas in this thesis most likely experienced MMI9-10, as the Round Top and Cascade rock avalanche fit in the size brackets (defined by Hancox, Perrin, and G.D. 2002) very large (1-50 x $10^6 m^3$) and extremely large (>50 x $10^6 m^3$), and have low-angle planes of failure. The relation to PGA is only approximate for this version of the MMI scale, with MMI 8-9 ranging from approx. 0.35g to 0.5g, and MMI 9-10 or greater from approx. 0.5g to 1g or greater (Hancox, Perrin, and G.D. 2002).

In conclusion, this work yields critical acceleration estimates of 0.85g (0.71-1g; -0.14/+0.15g) and 0.92g (0.66-1.17g: $\pm$ 25g) for the Cascade and Round Top rock avalanches respectively, which is in good agreement with the Bradley et al. (2017) simulation in Round Top's case, but somewhat higher for Cascade. However, actual PGA values will, according to this work, be higher than the critical acceleration estimates, as the latter is simply the threshold that the PGA must exceed, for an extended amount of time, in order to produce slope failure.

Near-field areas, like the case study areas used in this work, will most likely experience intensities of at least MMI 8, and quite possibly as high as MMI 10. Bradley et al. (2017) predict lower PGA values for the central part of Alpine

Fault; as PGAs can vary greatly from site to site, the results obtained in the present study cannot be extrapolated to this area. Hancox, Perrin, and G.D. 2002 notes that while PGA generally is considered a controlling parameter for co-seismic landslide initiation, long-duration shaking may have greater influence in producing very large landslides and higher MMIs. The highest PGAs in an earthquake strong-motion record are generally on the higher end of the frequency spectrum; long-period motion is thus under-represented in the Newmark model. This is an important limitation for the present study, as shaking produced by an Alpine Fault earthquake may last for longer than three minutes (Holden 2014).Nevertheless, this work represents a useful geological constraint for future ground motion simulations.

5 Conclusions and future work

- The Alpine Fault is a major plate boundary fault late in its earthquake cycle. It has a 29% chance of producing a M_W 7-8 earthquake in the next 50 years.
- Such an earthquake will cause extensive and widespread damage, especially on the West Coast, where abundant landsliding is one of the hazards expected.
- This work provides first-time geological constraints for an Alpine Fault earthquake, by using a modified version of the Newmark model, introduced in this study, on two pre-historic landslides, the Cascade and Round Top rock avalanches.
- The model yields a critical acceleration estimate of 0.85g (-0.14/+0.15g) for Cascade, and 0.92g ($\pm$ 25g) for Round Top.
- Possibilities for future work include using synthetic seismograms from Alpine Fault simulations, or real seismograms from suitable earthquakes, to produce Newmark displacements for the two landslides.
- Another opportunity for future work is using the remaining sections at each landslide site to estimate the maximum PGA for an Alpine Fault earthquake; these sections still being intact, but having slipped along their respective sackungen (at least in the case of Cascade), suggests that the shaking has been strong, but not strong enough to produce the catastrophic failure of these sections.

Bibliography

ARANZ Geo (2017). *3D Geological Modelling | Implicit Modelling | Geology Software | Leapfrog*. URL: https://www.leapfrog3d.com/.

Barth, N.C. (2014). The Cascade rock avalanche: implications of a very large Alpine Fault-triggered failure, New Zealand. *Landslides* 11, pp. 327–341. DOI: 10.1007/s10346-013-0389-1.

Bell, J.M. and C. Fraser (1906). The geology of the Hokitika sheet, North Westland quadrangle. *New Zealand Geological Survey Billetin*.

Berryman, K., S Beanland, et al. (1992). The Alpine Fault, New Zealand: Variation in Quaternary structural style and geomorphic expression. *Annales Tectonicae* VI, pp. 126–163.

Berryman, K., U. Cochran, et al. (2012). Major Earthquakes Occur Regularly on an Isolated Plate Boundary Fault. *Science* 336, pp. 1690–1693.

Bradley, B. A. et al. (2017). Ground motion simulations of great earthquakes on the Alpine Fault: effect of hypocentre location and comparison with empirical modelling. *New Zealand Journal of Geology and Geophysics* 60.3, pp. 188–198. DOI: 10.1080/00288306.2017.1297313.

Byerlee, J.D. (1968). Brittle-ductile transition in rocks. *Journal of Geophysical Research* 73 (14), pp. 4741–4750. DOI: 10.1029/JB073i014p04741.

California Geological Survey (2008). Guidelines for Evaluating and Mitigating Seismic Hazards in California. *California Geological Survey Special Publication* 117A.

Chigira, M., W.N. Wang, et al. (2003). Geological causes and geomorphological precursors of the Tsaoling landslide triggered by the 1999 Chi-Chi Earthquake, Taiwan. *Engineering Geology* 68, pp. 259–273.

Chigira, M., Xiyong Wu, et al. (2010). Landslides induced by the 2008 Wenchuan earthquake, Sichuan, China. *Geomorphology* 118, pp. 225–238.

Cochran, U.A. et al. (2017). A plate boundary earthquake record from a wetland adjacent to the Alpine fault in New Zealand refines hazard estimates. *Earth and Planetary Science Letters* 464.Supplement C, pp. 175–188. DOI: https://doi.org/10.1016/j.epsl.2017.02.026.

Columbus, J., P. Sirguey, and R. Tenzer (2011). A free, fully assessed 15-m DEM for New Zealand. *Survey Quarterly* 66, pp. 16–19.

Cooper, Alan and Richard J. Norris (1995). Displacement on the Alpine Fault at Haast River, South Westland, New Zealand. *New Zealand Journal of Geology and Geophysics* 38, pp. 509–514.

Cox, S.C., C.D. Menzies, et al. (2015). Changes in hot spring temperature and hydrogeology of the Alpine Fault hanging wall, New Zealand, induced by distal South Island earthquakes. *Geofluids* 15.1-2, pp. 216–239. DOI: 10.1111/gfl.12093.

Cox, S.C., M.W. Stirling, et al. (2012). Potentially active faults in the rapidly eroding landscape adjacent to the Alpine Fault, central Southern Alps, New Zealand. *Tectonics* 31.2. TC2011. DOI: 10.1029/2011TC003038.

Donahue, J. and N. Abrahamson (2014). Simulation-Based Hanging Wall Effects. *Earthquake Spectra* 30, pp. 1269–1284.

Escartín, J., G. Hirth, and B. Evans (2001). Strength of slightly serpentinized peridotites: Implications for the tectonics of oceanic lithosphere. *Geology* 29.11, pp. 1023–1026. ISSN: 0091-7613. DOI: 10.1130/0091-7613(2001)029\<1023:SOSSPI\>2.0.CO;2.

Fossen, H. (2010). *Structural Geology*. Cambridge University Press. DOI: 10.1017/CBO9780511777806.

Goodman, R.E. and H.B. Seed (1966). Earthquake-induced displacements in sand embankments. *Journal of the Soil Mechanics and Foundations Division* 92, pp. 125–146.

Hancox, G.T., N.D. Perrin, and Dellow G.D. (2002). Recent studies of historical earthquake-induced landsliding, ground damage, and MM intensity in New Zealand. *Bull NZ Soc Earthq Eng* 35 (2), pp. 59–95.

Handwerger, A.L. et al. (2016). Rate-weakening friction characterizes both slow sliding and catastrophic failure of landslides. *Proceedings of the National Academy of Sciences of the United States of America* 113 (37), pp. 10281–10286. DOI: http://doi.org/10.1073/pnas.1607009113.

Hirth, G. and S. Guillot (2013). Rheology and Tectonic Significance of Serpentinite. *Elements* 9.2, pp. 107–113. ISSN: 1811-5209. DOI: 10.2113/gselements.9.2.107.

Holden, C. (2014). *Ground motion modelling of an Alpine fault earthquake and a Hope fault earthquake for main South Island cities (NZ)*. Consultancy report 257. GNS Science. 24 p.

Howarth, J. et al. (2012). Lake sediments record cycles of sediment flux driven by large earthquakes on the Alpine Fault, New Zealand. *Geology* 40.

Ikari, M.J., C. Marone, and D.M. Saffer (2011). On the relation between fault strength and frictional stability. *Geology* 39.1, pp. 83–86. DOI: 10.1130/G31416.1.

Jibson, R.W. (2011). Methods for assessing the stability of slopes during earthquakes — A retrospective. *Engineering Geology* 122, pp. 43–50.

Kawano, Seiya, Ikuo Katayama, and Keishi Okazaki (2011). Permeability anisotropy of serpentinite and fluid pathways in a subduction zone. *Geology* 39.10, pp. 939–942. ISSN: 0091-7613. DOI: 10.1130/G32173.1.

Kohli, A.H. et al. (2011). Flash weakening of serpentinite at near-seismic slip rates. *Journal of Geophysical Research: Solid Earth* 116.B3. B03202. ISSN: 2156-2202. DOI: 10.1029/2010JB007833.

Korup, O. (2005). Large landslides and their effect on sediment flux in South Westland, New Zealand. *Earth Surface Processes and Landforms* 30, pp. 305–323.

Korup, O., M.J. McSaveney, and T. Davies (2004). Sediment generation and delivery from large historic landslides in the Southern Alps, New Zealand. *Geomorphology*, pp. 189–207.

Lee, W.G., P.N. Johnson, and P. Wardle (1983). *Botantical notes on the Upper Cascade River Valley, South Westland*. Botany Division Report. Department of Scientific and Industrial Research, Dunedin, New Zealand, 42 p.

Meunier, Patrick, Niels Hovius, and A. John Haines (2007). Regional patterns of earthquake-triggered landslides and their relation to ground motion. *Geophysical Research Letters* 34.20. L20408. DOI: 10.1029/2007GL031337.

Morrow, C.A., L.Q. Shi, and J.D. Byerlee (1982). Strain hardening and strength of clay-rich fault gouges. *Journal of Geophysical Research: Solid Earth* 87.B8, pp. 6771–6780. ISSN: 2156-2202. DOI: 10.1029/JB087iB08p06771.

Nathan, S., M.S. Rattenbury, and R.P. Suggate, comp. (2002). *Geology of the Greymouth area*. Institute of Geological & Nuclear Sciences 1:250 000 geological map 12. Lower Hutt, New Zealand: Institute of Geological & Nuclear Sciences Limited. 1 sheet + 58 p.

Newmark, N.M. (1965). Effects of earthquakes on dams and embankments. *Geotechnique* 15 (2), pp. 139–159.

Pasuto, A. and M. Soldati (1996). "Landslide hazard". In: *Environmental geomorphology*. Ed. by M. Panizza. Elsevier, pp. 64–68.

Romeo, R. (2000). Seismically induced landslide displacements: A predictive model. *Engineering Geology* 58, pp. 337–351.

Stirling, M. et al. (2012). National Seismic Hazard Model for New Zealand: 2010 Update. *Bulletin of the Seismological Society of America* 102.4, pp. 1514–1542. DOI: 10.1785/0120110170.

Sundberg, M., G. Hirth, and P. B. Kelemen (2010). Trapped Melt in the Josephine Peridotite: Implications for Permeability and Melt Extraction in the Upper Mantle. *Journal of Petrology* 51.1-2, pp. 185–200. DOI: 10.1093/petrology/egp089.

Sutherland, R., D. Eberhart-Phillips, et al. (2007). "Do Great Earthquakes Occur on the Alpine Fault in Central South Island, New Zealand?" In: *A Continental Plate Boundary: Tectonics at South Island, New Zealand*. Ed. by D. Okaya, T. Stern, and F. Davey. American Geophysical Union, pp. 235–251. ISBN: 9781118666142. DOI: 10.1029/175GM12.

Sutherland, R., S. Nathan, and I.M. Turnbull (1995). Pliocene–Quaternary sedimentation and Alpine Fault related tectonics in the lower Cascade Valley, South Westland, New Zealand. *New Zealand Journal of Geology and Geophysics* 38, pp. 431–450.

Sutherland, R., V.G. Toy, et al. (2012). Drilling reveals fluid control on architecture and rupture of the Alpine fault, New Zealand. *Geology* 40.12, p. 1143. DOI: 10.1130/G33614.1.

Sutherland, Rupert, Fred Davey, and John Beavan (2000). Plate boundary deformation in South Island, New Zealand, is related to inherited lithospheric structure. *Earth and Planetary Science Letters* 177.3, pp. 141–151. DOI: https://doi.org/10.1016/S0012-821X(00)00043-1.

Townend, John (2009). Drilling, Sampling, and Monitoring the Alpine Fault: Deep Fault Drilling Project—Alpine Fault, New Zealand; Franz Josef, New Zealand, 22–28 March 2009. *Eos, Transactions American Geophysical Union* 90.36, pp. 312–312. DOI: 10.1029/2009EO360004.

Tsaparli, Vasiliki et al. (2016). Vertical ground motion and its effects on liquefaction resistance of fully saturated sand deposits. *Proceedings of the Royal Society of London A: Mathematical, Physical and Engineering Sciences* 472.2192. DOI: 10.1098/rspa.2016.0434.

Turner, F.J. (1930). Physiographic features of the Lower Cascade Valley and the Cascade Plateau, South Westland. *Trans Proc R Soc NZ 1868–1961*.

Warren, G. (1967). *Sheet 17—Hokitika. Geological map of New Zealand 1:250,000*. Wellington, New Zealand: Department of Scientific and Industrial Research.

Wartman, J., J.D. Bray, and R.B. Seed (2003). Inclined plane studies of the Newmark sliding block procedure. *Journal of Geotechnical and Geoenvironmental Engineering* 129, pp. 673–684.

Wartman, J., R.B. Seed, and J.D. Bray (2005). Shaking table modeling of seismically induced deformations in slopes. *Journal of Geotechnical and Geoenvironmental Engineering* 131, pp. 610–622.

Westland District Council (2017). *Digitial Elevation Model (DEM) supplied by Westland District Council. DEM was generated from 0.3m GSD stereo imagery captured during February/March 2017. It has a point spacing of 9m with accuracy of plus/minus 0.6m 95% confidence level in clear open areas. Accuracy not guaranteed over dense vegetated areas.*

Wilson, R.C. and D.K. Keefer (1983). Dynamic analysis of a slope failure from the 6 August 1979 Coyote Lake, California, earthquake. *Bulletin of the Seismological Society of America* 73, pp. 863–877.

Worden, C.B. et al. (2012). Probabilistic Relationships between Ground-Motion Parameters and Modified Mercalli Intensity in California. *Bulletin of the Seismological Society of America* 102 (1), pp. 204–221.

Wright, C.A. (1998). The AD 930 long-runout Round Top debris avalanche, Westland, New Zealand. *New Zealand Journal of Geology and Geophysics* 41, pp. 493–497.

Yetton, M. D., A. Wells, and N. J. Traylen (1998). *The probability and consequences of the next Alpine Fault earthquake*. research report. 95/193. The Earthquake Commision (EQC).

Appendix A Source code: Spatial analysis for the Cascade rock avalanche

```
% Cascade profile analysis

% Along fall line at 315 degrees, extracted from ArcGIS

% Import xlsx file - first profile length then height
filename = 'Cascade accurate profile data.xlsx';
sheet = 1;
xlRange = 'A2:A160';

alongprofile = xlsread(filename,sheet,xlRange);

xlRange = 'B2:B160';

profileheight = xlsread(filename,sheet,xlRange);

%% Calculate beta

% Beta starting point (estimated from profile graph): (85.47, 599)

beta = 65; % in degrees, +- margin of error
slopeb = -tand(beta);
```

```
22
23 % Input starting point for line
24 Bx = 85.47;
25 By = 599;
26 yintb = Bx*tand(beta)+By;
27 xb = 85.47:300;
28 betafunc = slopeb*xb+yintb;
29
30 % Margin of error
31
32 betap5 = beta+5;
33 betam5 = beta-5;
34
35 slopebp5 = -tand(betap5);
36 yintbp5 = Bx*tand(betap5)+By;
37 xbp5 = Bx:250;
38 betap5func = slopebp5*xbp5+yintbp5;
39
40 slopebm5 = -tand(betam5);
41 yintbm5 = Bx*tand(betam5)+By;
42 xbm5 = Bx:350;
43 betam5func = slopebm5*xbm5+yintbm5;
44
45 % % Plot % (want to see beta only? Uncomment and run section)
46 % plot(xb,betafunc,'g')
47 % axis equal
48 % hold on
49 % plot(Bx,By,'*')
50 % plot(xbp5,betap5func,'k:')
51 % plot(xbm5,betam5func,'k:')
52 % legend('beta','beta point','beta + 5','beta - 5')
53
```

```
%% Calculate alpha

% Alpha at 8.5 degrees, parallel to slope above
alpha = 8.5; %8.5;
slopea = -tand(alpha);
% Input starting point for line
Ax = 1913;   % from profile
Ay = 38.8;  % from profile
yinta = Ax*tand(alpha)+Ay;
xa = 100:1913;
alphafunc = slopea*xa+yinta;

% Margin of error

alphap25 = alpha+2.5;
alpham25 = alpha-2.5;

slopeap25 = -tand(alphap25);
yintap25 = Ax*tand(alphap25)+Ay;
xap25 = 100:Ax;
alphap25func = slopeap25*xap25+yintap25;

slopeam25 = -tand(alpham25);
yintam25 = Ax*tand(alpham25)+Ay;
xam25 = 100:Ax;
alpham25func = slopeam25*xam25+yintam25;

% % Plot (uncomment and run section to only plot alpha)
% plot(xa,alphafunc,'r')
% axis equal
% hold on
% plot(Ax,Ay,'*')
```

```
% plot(xap25,alphap25func,'k--')
% plot(xam25,alpham25func,'k--')
% legend('alpha','alpha point','alpha + 2.5','alpha - 2.5')


%% Plot

f0 = figure;

plot(alongprofile,profileheight,'k','LineWidth',2) % Color was c
hold on

% Alpha and 2.5 margin of error
plot(xa,alphafunc,'r','LineWidth',1.5)
plot(xap25,alphap25func,'--k')

% Beta and margin of error
plot(xb,betafunc,'g','LineWidth',1.5)
plot(xbp5,betap5func,'k:','LineWidth',1)

plot(xbm5,betam5func,'k:','LineWidth',1)

% Alpha's lower margin of error (placed here for legend order purposes)
plot(xam25,alpham25func,'--k')

axis equal
axis([0,2400,0,1000])
title('Profile of the Cascade rock avalanche')
xlabel('Along profile (m)')
ylabel('Height (m)')
legend('Fall line profile','alpha (8.5)','Margin of error ( pm  2.5)',' beta  (65)',
hold off
```

Appendix B Source code: Spatial analysis for the Round Top rock avalanche

```
% Round Top profile analysis

% Import profile data

% Set range

R1 = 3;
C1 = 0;
C2 = 1;

R2 = 522;
R3 = 592;
R4 = 534;
R5 = 568;
R6 = 164;

FLm = dlmread('9m DEM fall line profile.txt',',',[R1 C1 R2 C1]);
FLh = dlmread('9m DEM fall line profile.txt',',',[R1 C2 R2 C2]);

NEm = dlmread('9m DEM NE profile.txt',',',[R1 C1 R3 C1]);
NEh = dlmread('9m DEM NE profile.txt',',',[R1 C2 R3 C2]);
```

```
22
23 SWm = dlmread('9m DEM SW profile.txt',' ',[R1 C1 R4 C1]);
24 SWh = dlmread('9m DEM SW profile.txt',' ',[R1 C2 R4 C2]);
25
26 SW2m = dlmread('9m DEM SW profile 2.txt',' ',[R1 C1 R5 C1]);
27 SW2h = dlmread('9m DEM SW profile 2.txt',' ',[R1 C2 R5 C2]);
28
29
30 %% Base line
31
32 % Points
33 % BP1 = (3705, 52.01);
34 % BP2 = (5400, 38.31);
35 BP1x = 3705;
36 BP1y = 52.01;
37 BP2x = 5400;
38 BP2y = 38.31;
39
40 slope = (BP2y-BP1y)/(BP2x-BP1x);
41 yint = BP1x*(-slope)+BP1y;
42 xbl = 0:4000;
43 Baselinefunc = slope*xbl+yint;
44
45 % Trigonometry for NE profile and base line intersect
46 trig1x = 762.3; %lower 1075;
47 trig1y = 331.7; %lower 192;
48 trig2x = 946; %1010; %lower 1148;
49 trig2y = 243.9; %219.9; %lower 132.8;
50
51 slopetrig = (trig2y-trig1y)/(trig2x-trig1x);
52 yinttrig = trig1x*(-slopetrig)+trig1y;
53 xtrig = 0:1500;
```

```
54 trigfunc = slopetrig*xtrig+yinttrig;
55
56 % Fall line fan profile - find the slope tangents
57 flu1x = 889;  flu1y = 284.8;  % Where flu = fall line upper
58 flu2x = 1160; flu2y = 206.4;
59
60 slopeflu = (flu2y-flu1y)/(flu2x-flu1x);
61 yintflu = flu1x*(-slopeflu)+flu1y;
62 xflu = 800:0.5:1400;
63 flufunc = slopeflu*xflu+yintflu;
64
65 fll1x = 1440;  fll1y = 141.2;  % Where fll = fall line lower
66 fll2x = 1643;  fll2y = 108.2;
67
68 slopefll = (fll2y-fll1y)/(fll2x-fll1x);
69 yintfll = fll1x*(-slopefll)+fll1y;
70 xfll = 1200:0.5:1800;
71 fllfunc = slopefll*xfll+yintfll;
72
73 plot(xbl,Baselinefunc,BP1x,BP1y,'*')
74 axis equal
75 hold on
76 plot(FLm,FLh,'c')
77 plot(NEm,NEh)
78 plot(xtrig,trigfunc)
79 plot(xflu,flufunc)
80 plot(xfll,fllfunc,'k')
81
82 % Lower NE profile fit gives intersect at (1223, 72)
83 % Upper NE profile fit gives intersect at (1340, 71)
84 % Up 2  NE profile fit gives intersect at (1307, 71.4)
85 % Fall line fan slopes give  intersect at (1315, 161.5)
```

```
86
87 %% Calculate beta function
88
89 % Beta point = (86.96, 779.5) --> ca. vendepunkt paa fallineprofil
90 beta = 65; % in degrees, +- margin of error
91 slopeb = -tand(beta); % a in ax + b for 60 degrees
92 % Input starting point for line
93 Bx = 86.96;
94 By = 779.5;
95 yintb = Bx*tand(beta)+By;
96 xb = 86.96:390; % Determined by combined margins of error of alpha and beta for plot
97 betafunc = slopeb*xb+yintb;
98
99 % Margin of error
100
101 betap5 = beta+5;
102 betam5 = beta-5;
103
104 slopebp5 = -tand(betap5);
105 yintbp5 = Bx*tand(betap5)+By;
106 xbp5 = Bx:323;
107 betap5func = slopebp5*xbp5+yintbp5;
108
109 slopebm5 = -tand(betam5);
110 yintbm5 = Bx*tand(betam5)+By;
111 xbm5 = Bx:465;
112 betam5func = slopebm5*xbm5+yintbm5;
113
114 % % Plot
115 % plot(xb,betafunc,'g')
116 % axis equal
117 % hold on
```

```
118 % plot(Bx,By,'*')
119 % plot(xbp5,betap5func,'k:')
120 % plot(xbm5,betam5func,'k:')
121 % legend('beta','beta point','beta + 5','beta - 5')
122
123 %% Calculate alpha function
124
125 % Alpha, 10 degrees
126 alpha = 10; %8.5;
127 slopea = -tand(alpha);
128 % Input starting point for line
129 Ax = 1315;   % from fall line fan slope angle intersect
130 Ay = 71.33;  % from base line y value at above intersect
131 yinta = Ax*tand(alpha)+Ay;
132 xa = 200:1315;  % For plot prettiness purposes
133 alphafunc = slopea*xa+yinta;
134 plot(xa,alphafunc,Ax,Ay,'*')
135 axis equal
136
137 % Margin of error
138
139 alphap5 = alpha+5;
140 alpham5 = alpha-5;
141
142 slopeap5 = -tand(alphap5);
143 yintap5 = Ax*tand(alphap5)+Ay;
144 xap5 = 200:Ax;
145 alphap5func = slopeap5*xap5+yintap5;
146
147 slopeam5 = -tand(alpham5);
148 yintam5 = Ax*tand(alpham5)+Ay;
149 xam5 = 200:Ax;
```

```
150 alpham5func = slopeam5*xam5+yintam5;
151
152 % Add p10 just to see what it looks like
153 alphap10 = alpha+10;
154
155 slopeap10 = -tand(alphap10);
156 yintap10 = Ax*tand(alphap10)+Ay;
157 alphap10func = slopeap10*xa+yintap10;
158
159 % % Plot
160 % plot(xa,alphafunc,'r')
161 % axis equal
162 % hold on
163 % plot(Ax,Ay,'*')
164 % plot(xap5,alphap5func,'k:')
165 % plot(xam5,alpham5func,'k:')
166 % plot(xa,alphap10func,'k--')
167 % legend('alpha','alpha point','alpha + 5','alpha - 5')
168
169 %% Plotting
170
171 f1 = figure;
172 plot(FLm,FLh,'c','LineWidth',2)
173 axis equal
174 axis([0,5410,0,2500])
175 hold on
176 plot(NEm,NEh,'--','Color',[0.91 0.41 0.17],'LineWidth',0.5)
177 plot(SWm,SWh,'--g','Color',[0.7 0 0.6],'LineWidth',0.5)
178 plot(SW2m,SW2h,'--','Color',[0.4 0.3 0.7],'LineWidth',0.5)
179
180 plot(xa,alphafunc,'r','LineWidth',1.5)
181 plot(xb,betafunc,'g','LineWidth',1.5)
```

```
182
183 plot(xbl,Baselinefunc,'Color',[0.5 0.5 0.5],'LineWidth',1)
184 % plot(xtrig,trigfunc)
185 % plot(xflu,flufunc)
186 % plot(xfll,fllfunc)
187
188 plot(xap5,alphap5func,'k:','LineWidth',1)
189 plot(xam5,alpham5func,'k:','LineWidth',1)
190 % plot(xa,alphap10func,'k--')
191
192 plot(xbp5,betap5func,'k:','LineWidth',1)
193 plot(xbm5,betam5func,'k:','LineWidth',1)
194
195 legend('Fall line profile','NE','SW1','SW2','alpha','beta','Base line','Margins of
196
197 title('Profiles of the Round Top Avalanche')
198 xlabel('Along profile (m)')
199 ylabel('Profile height (m)')
```

Appendix C Source code: Factor of Safety and critical acceleration for the Cascade rock avalanche

```
% Cascade Newmark Calculations

% Written in MATLAB 2017a on a Windows 10 computer, by Astrid Vetrhus

% % Define and calculate constants

rho=3200;   %in kg/m^3
g=9.81;     %in m/s^2

n = 101;      % No. of elements in vectors - must be an odd number
% for vector to include the median. 101 is a good number.


% Volume and weight

V = 750*10e+6; % in m3 (Barth 2014)
sW = V*rho*g; % weight in N
% (Volume does not really matter, as it cancels out of FoS equation)
```

```
% Define variables


% Lower slope (alpha)
% Median at 8.5 degrees (parallel to part of fall line profile), margin of error +


sa = 8.5;       % Static alpha
moea = 5;       % Vary alpha - for margin of error
moeas = 2.5;    % Smaller margin of error, the main MoE used for Cascade
va = transpose(linspace(sa-moeas ,sa+moeas, n));

vabetsoff = transpose(linspace(sa+moea, sa-moea, n));
vabetsoffs = transpose(linspace(sa+moeas, sa-moeas, n));

% Upper slope (sackung; beta)
% About 60-70 degrees (Barth 2014) -> median 65, range +- 5
sb = 65;
moeb = 5;
vb = transpose(linspace(sb-moeb, sb+moeb, n));
vbbetsoff = transpose(linspace(sb+moeb, sb-moeb, n));

% Friction
% Serpentinite coefficient of friction and margin of error from Reinen (?)
su = 0.65;
moeu = 0.05;
vu = transpose(linspace(su-moeu, su+moeu, n));
vubetsoff = transpose(linspace(su-moeu, su+moeu, n));

%FoS = Factor of Safety
FoSa = zeros(n,1);
FoSb = zeros(n,1);
FoSu = zeros(n,1);
FoSW = zeros(n,1);
```

```
FoSbetsoff = zeros(n,1);

FoSbetsoffs = zeros(n,1);


% ac = Critical acceleration

aca = zeros(n,1);

acb = zeros(n,1);

acu = zeros(n,1);

acW = zeros(n,1);

acbetsoff = zeros(n,1);

acbetsoffs = zeros(n,1);



% Modified Newmark

% Vary alpha

for i=1:n

FoSa(i) = (su*sW*cosd(va(i)) + su*sW*cosd(sb - va(i)))/...

(sW*sind(va(i)));

end


for j=1:n

aca(j) = (FoSa(j)-1)*g*sind(va(j));

end


% Vary beta

for i=1:n

FoSb(i) = (su*sW*cosd(sa) + su*sW*cosd(vb(i)-sa)) /...

(sW*sind(sa));

end


for j=1:n

acb(j) = (FoSb(j)-1)*g*sind(sa);

end
```

```
% Vary mu
for i=1:n
FoSu(i) = (vu(i)*sW*cosd(sa) + vu(i)*sW*cosd(sb - sa)) /...
(sW*sind(sa));
end

for j=1:n
acu(j) = (FoSu(j)-1)*g*sind(sa);
end



% All bets are off - everything changes!
% FoS
% Alpha +-5 degrees
for i=1:n
FoSbetsoff(i) = (vubetsoff(i)*sW*cosd(vabetsoff(i)) + vubetsoff(i)*sW*cosd(vbbetsc
(sW*sind(vabetsoff(i)));
end

% Alpha +-2.5 degrees
for i=1:n
FoSbetsoffs(i) = (vubetsoff(i)*sW*cosd(vabetsoffs(i)) + vubetsoff(i)*sW*cosd(vbbet
(sW*sind(vabetsoffs(i)));
end

% Critical acceleration
% Alpha +-5 degrees
for j=1:n
acbetsoff(j) = (FoSbetsoff(j)-1)*g.*sind(vabetsoff(j));
end
```

```
% Alpha +-2.5 degrees
for j=1:n
acbetsoffs(j) = (FoSbetsoffs(j)-1)*g.*sind(vabetsoffs(j));
end

% Convert to units of g
vaacg = aca / g;
vbacg = acb / g;
vuacg = acu / g;
acbetsoffg = acbetsoff / g;
acbetsoffsg = acbetsoffs / g;



% Plot
x=linspace(0,n-1,n);
xtx = 0:10:100;
y = ones(length(x));

f1=figure;
plot(x,FoSa,'r')
hold on
plot(x,FoSb,'g')
plot(x,FoSu,'k')
plot(x,y,'Color',[0.5 0.5 0.5])
title('Model sensitivity: Factor of Safety')
xlabel('Index')
ylabel('Factor of Safety')
xlim([x(1) x(end)])
ylim([0,16])
% text(median(x)-10,median(FoSa)+1,['Median = ',num2str(median(FoSa))])
legend('alpha varies (8.5 pm 2.5)','beta varies (65 pm 5)','mu varies (0.65 pm 0.05)
xticks([])
```

```
f1.PaperUnits = 'centimeters';
f1.PaperPosition = [0 0 7.4 7];
hold off

f2=figure;
plot(x,vaacg,'r')
hold on
plot(x,vbacg,'g')
plot(x,vuacg,'k')
title('Model sensitivity: Critical acceleration')
xlabel('Index')
ylabel('Critical acceleration (g)')
xlim([x(1) x(end)])
ylim([0.6 1.2])
legend('alpha varies (8.5 pm 2.5)','beta varies (65 pm 5)','mu varies (0.65 pm 0.0
xticks([])
f2.PaperUnits = 'centimeters';
f2.PaperPosition = [0 0 7.4 7];
hold off

f3=figure;
% plot(x,FoSbetsoff,'Color',[0.5 0.5 0.5])
plot(x,FoSbetsoffs,'b')
hold on
plot(x,y,'Color',[0.5 0.5 0.5])
title({'Factor of Safety with margin of error,'; 'as a function of alpha, beta, an
xlabel('Index')
ylabel('Factor of Safety')
xlim([x(1) x(end)])
ylim([0,16])
% xticks([x(1) median(x) x(end)])
%xticklabels(xt)
```

```
% legend('Margin of error of alpha is (pm5)','Margin of error of alpha is (pm 2.5)',
legend(['Total range of ', newline, 'the Factor of Safety'],'Location','northwest')
xticks([])
f3.PaperUnits = 'centimeters';
f3.PaperPosition = [0 0 7.4 7];
hold off


f4=figure;
% plot(x,acbetsoffg,'Color',[0.5 0.5 0.5])
plot(x,acbetsoffsg,'b')
hold on
title({'Critical acceleration with margin of error,'; 'as a function of the FoS and a
xlabel('Index')
ylabel('Critical acceleration (g)')
xlim([x(1) x(end)])
ylim([0.6 1.2])
legend(['Total range of ', newline, 'the critical acceleration'],'Location','northwes
xticks([])
f4.PaperUnits = 'centimeters';
f4.PaperPosition = [0 0 7.4 7];
hold off
```

Appendix D Source code: Factor of Safety and critical acceleration for the Round Top rock avalanche

```
% % Round Top Newmark Calculations

% Written in MATLAB 2017a on a Windows 10 computer, by Astrid Vetrhus

% % Define and calculate constants and the volume variable

rho=2757;   %in kg/m^3 - mylonite mean from digital rock density map NZ paper
g=9.81;     %in m/s^2

n = 101;      % No. of elements in vectors - must be an odd number
% for vector to include the median


% % Volume and weight

% W cancels out of FoS equation
```

```
% Mean 45*10^6 m^3, margin of error +- 28 (Wright 1998)

V = 45*10e+6;         % in m^3

sW = V*rho*g;        % weight in N



% Define variables

% Lower slope (alpha)
% Median at 10 degrees, margin of error +- 5

sa = 10;         % Static alpha
moea = 5;        % Margin of error
moeas = 2.5;     % Smaller margin of error, used for Cascade

% Model sensitivity
va = transpose(linspace(sa-moea ,sa+moea, n));

% Total range
vabetsoff = transpose(linspace(sa+moea, sa-moea, n));
vabetsoffs = transpose(linspace(sa+moeas, sa-moeas, n));

% Upper slope (sackung; beta)
% Dips 60-70 degrees; median 65 and range +- 5
sb = 65;
moeb = 5;
vb = transpose(linspace(sb-moeb, sb+moeb, n));
vbbetsoff = transpose(linspace(sb+moeb, sb-moeb, n));

% Coefficient of friction
% Standard crustal rock at 0.7
```

```
su = 0.7;
moeu = 0.1; % was 0.05, but that's prob too narrow
vu = transpose(linspace(su-moeu, su+moeu, n));
vubetsoff = transpose(linspace(su-moeu, su+moeu, n));

%FoS = Factor of Safety
FoSa = zeros(n,1);
FoSb = zeros(n,1);
FoSu = zeros(n,1);
FoSW = zeros(n,1);
FoSbetsoff = zeros(n,1);
FoSbetsoffs = zeros(n,1);

% ac = Critical acceleration
aca = zeros(n,1);
acb = zeros(n,1);
acu = zeros(n,1);
acW = zeros(n,1);
acbetsoff = zeros(n,1);
acbetsoffs = zeros(n,1);



% Modified Newmark
% Vary alpha - adding -alpha
for i=1:n
FoSa(i) = (su*sW*cosd(va(i)) + su*sW*cosd(sb - va(i)))/...
(sW*sind(va(i)));
end

for j=1:n
aca(j) = (FoSa(j)-1)*g*sind(va(j));
end
```

```
% Vary beta
for i=1:n
FoSb(i) = (su*sW*cosd(sa) + su*sW*cosd(vb(i)-sa)) /...
(sW*sind(sa));
end

for j=1:n
acb(j) = (FoSb(j)-1)*g*sind(sa);
end

% Vary mu
for i=1:n
FoSu(i) = (vu(i)*sW*cosd(sa) + vu(i)*sW*cosd(sb - sa)) /...
(sW*sind(sa));
end

for j=1:n
acu(j) = (FoSu(j)-1)*g*sind(sa);
end



% All bets are off - everything changes!
% FoS
% Alpha +-5 degrees
for i=1:n
FoSbetsoff(i) = (vubetsoff(i)*sW*cosd(vabetsoff(i)) + vubetsoff(i)*sW*cosd(vbbetsoff
(sW*sind(vabetsoff(i)));
end

% Alpha +-2.5 degrees
for i=1:n
```

```
FoSbetsoffs(i) = (vubetsoff(i)*sW*cosd(vabetsoffs(i)) + vubetsoff(i)*sW*cosd(vbbet

(sW*sind(vabetsoffs(i)));

end


% Critical acceleration

% Alpha +-5 degrees

for j=1:n

acbetsoff(j) = (FoSbetsoff(j)-1)*g.*sind(vabetsoff(j));

end


% Alpha +-2.5 degrees

for j=1:n

acbetsoffs(j) = (FoSbetsoffs(j)-1)*g.*sind(vabetsoffs(j));

end


% Convert to units of g

vaacg = aca / g;

vbacg = acb / g;

vuacg = acu / g;

acbetsoffg = acbetsoff / g;

acbetsoffsg = acbetsoffs / g;



% Plot

x=linspace(0,n-1,n);

y = ones(length(x));



f1=figure;

plot(x,FoSa,'r')

hold on

plot(x,FoSb,'g')
```

```
plot(x,FoSu,'k')
plot(x,y,'Color',[0.5 0.5 0.5])  % FoS = 1
title('Model sensitivity: Factor of Safety')
xlabel('Index')
ylabel('Factor of Safety')
xlim([x(1) x(end)])
ylim([0,16])
legend('alpha varies (10 pm 5)','beta varies (65 pm 5)','mu varies (0.7 pm 0.1)','Loc
xticks([])
f1.PaperUnits = 'centimeters';
f1.PaperPosition = [0 0 7.4 7];
hold off

f2=figure;
plot(x,vaacg,'r')
hold on
plot(x,vbacg,'g')
plot(x,vuacg,'k')
title('Model sensitivity: Critical acceleration')
xlabel('Index')
ylabel('Critical acceleration (g)')
xlim([x(1) x(end)])
ylim([0.6 1.2])
legend('alpha varies (10 pm 5)','beta varies (65 pm 5)','mu varies (0.7 pm 0.1)','Loc
xticks([])
f2.PaperUnits = 'centimeters';
f2.PaperPosition = [0 0 7.4 7];
hold off

f3=figure;
plot(x,FoSbetsoff,'b')
hold on
```

```
plot(x,y,'Color',[0.5 0.5 0.5])
title({'Factor of Safety with margin of error,'; 'as a function of alpha, beta, an
xlabel('Index')
ylabel('Factor of Safety')
xlim([x(1) x(end)])
ylim([0,16])
xticks([])
legend(['Total range of ', newline, 'the Factor of Safety'],'Location','northwest'
f3.PaperUnits = 'centimeters';
f3.PaperPosition = [0 0 7.4 7];
hold off

f4=figure;
plot(x,acbetsoffg,'b')
hold on
title({'Critical acceleration with margin of error,'; 'as a function of the FoS an
xlabel('Index')
ylabel('Critical acceleration (g)')
xlim([x(1) x(end)])
ylim([0.6 1.2])

legend(['Total range of ', newline, 'the critical acceleration'],'Location','north
xticks([])
f4.PaperUnits = 'centimeters';
f4.PaperPosition = [0 0 7.4 7];
hold off
```